The seasonal cycle of δ13C of atmospheric carbon dioxide: Influences of land and ocean carbon fluxes and drivers.

Sebastian Lienert[1], Sönke Zaehle[2], and Fortunat Joos[3]

[1]University of Bern Physics Institute Climate and Environmental Physics & Oschger Centre for Climate Change Research
[2]Max Planck Institute for Biogeochemistry
[3]University of Bern

November 28, 2022

Abstract

In situ measurements of the seasonal cycle of δ13C(CO2) provide complementary information on the seasonality of the global carbon cycle, but are currently not exploited in the context of process-based carbon cycle models. We use isotope-enabled simulations of the Bern3D-LPX Earth System Model of Intermediate Complexity and fossil fuel emission estimates together with a model of atmospheric transport to simulate local atmospheric δ13C(CO2). We find good agreement between the measured and simulated seasonal cycle of atmospheric δ13C(CO2) (mean seasonal amplitude mismatch of 0.02 northern latitude sites. Factorial simulations reveal that the seasonal cycle of δ13C(CO2) is primarily driven by land biosphere carbon exchange. Spatial and temporal fluxes of CO2 and their signatures are analyzed to quantify the terrestrial drivers. The influence of external forcings (climate and land use change) on seasonal amplitude is found to be small. Unlike the growth of seasonal amplitude of CO2, no consistent change in seasonal amplitude of δ13C(CO2) is simulated over the historical period, nor evident in the available observations. We conclude that the seasonal cycle of δ13C(CO2) is influenced by different carbon cycle processes, and its potential as a novel atmospheric constraint should be further explored.

The seasonal cycle of δ^{13}C of atmospheric carbon dioxide: Influences of land and ocean carbon fluxes and drivers.

Sebastian Lienert[1,2], Sönke Zaehle[3], Fortunat Joos[1,2]

[1]Climate and Environmental Physics, University of Bern, Bern Switzerland
[2]Oeschger Centre for Climate Change Research, University of Bern, Bern, Switzerland
[3]Max Planck Institute for Biogeochemistry, P.O. Box 600164, Hans-Knöll-Str. 10, 07745 Jena, Germany

Key Points:

- We simulate local atmospheric $\delta^{13}C(CO_2)$ by transporting (TM3) fluxes from EMIC simulations (Bern3D-LPX) and fossil fuel emission estimates.
- Good agreement in the phase and amplitude of measured and modeled seasonal cycles of $\delta^{13}C(CO_2)$, with absent multi-decadal trends, is found.
- Factorial simulations reveal land biosphere fluxes as the main driver of $\delta^{13}C(CO_2)$ seasonality and small influences of climate and land use.

Corresponding author: Sebastian Lienert, sebastian.lienert@unibe.ch

Abstract

In situ measurements of the seasonal cycle of $\delta^{13}C(CO_2)$ provide complementary information on the seasonality of the global carbon cycle, but are currently not exploited in the context of process-based carbon cycle models. We use isotope-enabled simulations of the Bern3D-LPX Earth System Model of Intermediate Complexity and fossil fuel emission estimates together with a model of atmospheric transport to simulate local atmospheric $\delta^{13}C(CO_2)$. We find good agreement between the measured and simulated seasonal cycle of atmospheric $\delta^{13}C(CO_2)$ (mean seasonal amplitude mismatch of 0.02 ‰ across 19 sites), particularly at high northern latitude sites. Factorial simulations reveal that the seasonal cycle of $\delta^{13}C(CO_2)$ is primarily driven by land biosphere carbon exchange. Spatial and temporal fluxes of CO_2 and their signatures are analyzed to quantify the terrestrial drivers. The influence of external forcings (climate and land use change) on seasonal amplitude is found to be small. Unlike the growth of seasonal amplitude of CO_2, no consistent change in seasonal amplitude of $\delta^{13}C(CO_2)$ is simulated over the historical period, nor evident in the available observations. We conclude that the seasonal cycle of $\delta^{13}C(CO_2)$ is influenced by different carbon cycle processes, and its potential as a novel atmospheric constraint should be further explored.

1 Introduction

The seasonal variations in the carbon exchange fluxes between the atmosphere and the surface cause a seasonal cycle in atmospheric CO_2 (C_a) (Keeling et al., 1996; Graven et al., 2013; Masarie et al., 2014) and its stable isotopic signature ($\delta^{13}C_a$) (Keeling et al., 2005; GLOBALVIEW-CO2C13, 2009). These atmospheric seasonal cycles are dominated by exchange with the land biosphere in the Northern Hemisphere and the tropics, while atmosphere-ocean fluxes play a relevant role in the southern high latitudes. Observations of the atmospheric seasonal cycles provide information on the functioning of the carbon cycle and constraints for model evaluation (Heimann et al., 1989, 1998).

The anthropogenic combustion of fossil fuels perturbs the carbon cycle-climate system. It causes a long-term decrease in $\delta^{13}C_a$, in addition to rising CO_2 and global warming. The decrease, termed the Suess Effect (Suess, 1955; Keeling, 1979), is a consequence of the low isotopic ratios of coal, oil, and gas (Andres et al., 2009a). In addition, the release of isotopically depleted (or light) CO_2 to the atmosphere due to land use change further lowers $\delta^{13}C_a$. The isotopic perturbation in the atmosphere is moderated by the

exchange of the atmosphere with the land biosphere and ocean and is underlying the $\delta^{13}C_a$ seasonal cycle.

Carbon isotopic discrimination is the preferential transfer of light ^{12}C compared to heavier ^{13}C. Discrimination is different for the different physical, chemical, and biological processes (Mook, 1986) causing differences in the isotopic composition of carbon reservoirs and fluxes. Discrimination is particularly large during the assimilation of CO_2 from the atmosphere by plant photosynthesis. Discrimination is much larger for the C3 than the C4 photosynthetic pathway and influenced by environmental parameters (Farquhar, 1983, 1989; Lloyd & Farquhar, 1994; Brüggemann et al., 2011; Farquhar & Cernusak, 2012; Evans & Von Caemmerer, 2013; Walker et al., 2021). The $\delta^{13}C$ signature of the atmosphere-to-land biosphere carbon flux, affecting the $\delta^{13}C_a$ seasonal cycle, may change in response to changes in the distribution of C3 and C4 plants in agricultural or natural systems. Discrimination by individual plants may change due to changing CO_2, temperature, relative humidity, and water availability, though tree ring isotopic data indicate on average small changes over the last century (e.g., Saurer et al. (2014); Keller et al. (2017)).

The seasonal cycle of C_a and $\delta^{13}C_a$ are driven by the net uptake of carbon during the growing season, lowering C_a and increasing $\delta^{13}C_a$, and the net release of isotopically light carbon during the winter or dry season. The observed seasonal cycle and amplitude growth of C_a (Keeling et al., 1996; Graven et al., 2013) have been widely used to evaluate carbon cycle models and system understanding (Heimann et al., 1998; Dargaville et al., 2002; Scholze et al., 2008; Peng et al., 2015; Lienert & Joos, 2018) by transporting fluxes from terrestrial, oceanic, and fossil sources with a model of atmospheric transport, to obtain local C_a anomalies. Studies address the role of different climatic drivers and terrestrial carbon cycle processes such as drought, land use, warming, productivity or soil respiration (Heimann et al., 1989, 1998; Graven et al., 2013; Forkel et al., 2016; Ito et al., 2016; Bastos et al., 2019; Wang et al., 2020) and surface-to-atmosphere C fluxes (e.g. Peylin et al. (2013)).

Comparable studies are, to our knowledge, lacking for the seasonal cycle of $\delta^{13}C_a$. Such studies are also scarce for the carbon isotope ^{14}C (Turnbull et al., 2017). While in-situ atmospheric $\delta^{13}C_a$ measurements are available (GLOBALVIEW-CO2C13, 2009; Keeling et al., 2001), this seasonally-resolved data is yet to be fully utilized in the context

of processed-based carbon cycle models. Observations of $\delta^{13}C_a$ seasonal cycles have been used to investigate isotopic discrimination (Ballantyne et al., 2010) and trends in phenology (Gonsamo et al., 2017), but to our knowledge have not been used as a benchmark for model performance in combination with an atmospheric transport model. The comparison of modeled ^{13}C fluxes to in-situ observations is difficult because a transport model relies on the availability of spatial ^{13}C fluxes of land, ocean, and fossil fuel fluxes.

In this study, we present results on the use of in-situ $\delta^{13}C_a$ measurements as an observational constraint for a processed-based carbon cycle model. The simulated net atmosphere-to-surface spatial fluxes of CO_2 and $\delta^{13}C_a$ and their seasonality are discussed and used alongside gridded fossil fuel estimates to simulate atmospheric $\delta^{13}C_a$ using the matrix representation of an atmospheric transport model. The seasonal cycle of transported C_a and $\delta^{13}C_a$ are compared to in-situ atmospheric flask sampling observations, collected at various measurement stations across the globe (Cooperative Global Atmospheric Data Integration Project, 2013; Keeling et al., 2001; GLOBALVIEW-CO2C13, 2009). The overall ability of the model suite to reproduce global atmospheric C_a and $\delta^{13}C_a$ is evaluated. The dependence of the results on the used forcing data is evaluated with factorial experiments. Changes in seasonal amplitudes over the historical period are addressed. Finally, we discuss the viability of $\delta^{13}C_a$ seasonality as a novel observational constraint in the context of process-based carbon cycle models.

2 Methods

2.1 Bern3D-LPX

Spatially-resolved surface to atmosphere CO_2 and $^{13}CO_2$ fluxes are obtained by emission-driven simulations with the Earth system Model of Intermediate Complexity (EMIC) Bern3D-LPX. Here, the ocean-atmosphere model Bern3D (Jeltsch-Thömmes & Joos, 2020; Battaglia & Joos, 2018; Ritz et al., 2011) is coupled to the Dynamic Global Vegetation Model (DGVM) LPX-Bern v1.4 (Lienert & Joos, 2018). The Bern3D model features a 41 x 40 horizontal ocean resolution with 32 depth layers, coupled to a single-layer energy-moisture balance atmosphere (Ritz et al., 2011). The atmospheric carbon and carbon isotope inventories and CO_2 mixing ratio in dry air (C_a) and its $\delta^{13}C$ signature ($\delta^{13}C_a$) are tracked in a well-mixed box, with input and output from exchange fluxes with the ocean and land biosphere and fossil emissions. In Bern3D, carbon is im-

plemented as a tracer and features kinetic fractionation in air-sea gas exchange and the production of organic material and $CaCO_3$ (Menviel & Joos, 2012; Menviel et al., 2012, 2015; Jeltsch-Thömmes & Joos, 2020). We use the default model configuration of Bern3D with the addition of monthly output of air-sea CO_2 and $^{13}CO_2$ fluxes. LPX-Bern features coupled carbon, nitrogen, and water cycling and is run on a 3.75° x 2.5° resolution. Carbon isotopes were added to LPX-Bern early in its development (Scholze et al., 2003), using a photosynthetic fraction scheme (Lloyd & Farquhar, 1994). Assimilated carbon and isotopes are cycled, without further isotopic fractionation, through all vegetation, litter, soil, and product pools. The signature of respired carbon reflects the signature of carbon assimilated at previous times; the lag times between assimilation and respiration are dictated by the turnover time scales of the various pools (e.g. soil and vegetation carbon). The turnover time depends on environmental conditions (temperature and soil moisture).

LPX-Bern is tailored for computational efficiency for glacial-interglacial and large ensemble simulations. A number of fluxes, namely litterfall, carbon allocation from photosynthesis to biomass, light competition and background mortality, establishment, and fire disturbance, are computed only at the end of each model year. In earlier applications, these fluxes were added immediately to the carbon pools, causing a discontinuity in net atmosphere-land biosphere fluxes between January and December. Here, we distribute the end of year additions to carbon pools over the course of the year. For simplicity and in the absence of seasonal information for these fluxes, the additional carbon is distributed to the pools equally over all months in the following model year.

In the standard setup of LPX and TM3 (see next subsection), ^{13}C is represented in units of permil and mol permil (or gram-C permil) (Scholze et al., 2003). Alternatively, we represent ^{13}C in molar units in TM3 to check results for numerical accuracy. A three order of magnitude higher numerical precision is required to model ^{13}C in absolute, molar units, compared to the permil units.

We checked the Bern3D and LPX codes, and adjusted it to resolve small numerical inaccuracies. These adjustments had hardly any impact on modelled CO_2 and $\delta^{13}CO_2$ in Bern3D and LPX. Time-integrated global fluxes of CO_2 and $^{13}CO_2$ are compared to the total change in the C and ^{13}C inventories from all carbon pools in molar units. De-

viations are on the order of magnitude expected from errors relating to machine precision. Further, no significant model drift is observed in the control simulation.

The performance of the isotope module in LPX-Bern was recently compared to a global compilation of 20th-century carbon isotope tree ring records and carbon isotope measurements on leaves (Keller et al., 2017; Saurer et al., 2014). The model was found to be able to reasonably reproduce spatial patterns of δ^{13}C of C3 trees and match the observed changes in discrimination of C3 trees over the 20th century.

Bern3D and LPX-Bern were spun up individually, followed by a 500-year spinup with the coupled model to reach a pre-industrial (1700 CE; 276.3 ppm, -6.27 ‰) equilibrium. A transient simulation over the industrial period (1700 to 2020) is driven by annual fossil carbon emissions (including the contribution from cement production) (Friedlingstein et al., 2020), land use area changes, and non-CO_2 radiative forcing. The stable carbon isotopic signature of the fossil fuel emissions is taken from Andres et al. (2017), which spans 1751-2014. The signature was assumed to be constant for 1700-1751. For the period 2014 to 2020, signatures of major source categories (coal, oil, gas, cement) are assumed constant and combined with the emission sources from Friedlingstein et al. (2020), thereby following the approach of Andres et al. (2000). In earlier applications of LPX-Bern v1.4, the area fraction of C3 and C4 plants is determined dynamically based on bioclimatic limits and competition for resources. Here, we explicitly distinguish land use classes for C3 and C4 crops and prescribe their extent based on LUH2 (Hurtt et al., 2020).

The NCEP/NCAR monthly wind stress climatology (Kalnay et al., 1996) is prescribed to the ocean surface of Bern3D. Monthly climate fields from CRU-TS4.05 (Harris et al., 2020) are used for the climate of the land model. For the period 1700-1900 and the model spinup, the climate of the period 1901-1931 is recycled. Thus, the land, ocean, and atmospheric carbon cycle are prognostically coupled, while LPX is not coupled to the Bern3D climate fields. This approach assures that LPX is forced by the best available climatic information. The LUH2 land use changes (Hurtt et al., 2020) are used to prescribe net land use changes to LPX-Bern. Nitrogen deposition and fertilization are taken from the NMIP project (Tian et al., 2018).

Besides the standard simulation ($E_{standard}$), in which all the external forcings mentioned above are transient, factorial simulations were performed to evaluate model sensitivity. In simulation $E_{constclim}$, climate is kept constant by recycling the climate forc-

ing for the land and decoupling the physical model in Bern3D from changes in carbon inventory and albedo. Land use is kept at pre-industrial distribution in simulation E_{noLU}, and fossil carbon emissions are zero in simulation E_{noFF}. A control simulation ($E_{control}$) without anthropogenic CO_2 emissions and non-CO_2 radiative forcing, and constant land use, nitrogen deposition and fertilization at 1700 level, as well as recycling 1901-1931 land climate provides a baseline.

2.2 Atmospheric Transport Model TM3 and the seasonal cycles of CO_2 and $\delta^{13}C_a$

We employ the transport matrices of the TM3 atmospheric transport model (Heimann & Körner, 2003) originally published by Kaminski et al. (1998) and further applied and tested by Schürmann et al. (2016). The TM3 matrices are used to translate atmosphere-to-surface CO_2 fluxes ($F_{as,net}$) simulated by Bern3D-LPX, as well as estimated monthly fluxes from fossil fuel CO_2 emissions (Andres et al., 2009b) into local CO_2 anomalies at 19 measurement stations across the globe. Prior to transport, the fluxes are remapped to the TM3 72x48 grid ($5^o \times 3.75^o$).

By applying Jacobi matrices the gridded fluxes are translated into local anomalies. Here, the matrices span from 1982 to 2012 and are only available if there is also a CO_2 measurement available at the corresponding station. Each matrix represents the sensitivity of the local atmospheric concentration for a given month to the local surface fluxes of the previous period, spanning up to 48 months. For example, the seasonal anomaly in September 1986 is influenced by surface-atmosphere fluxes from October 1982 to September 1986, where most of the information is typically from a few months preceding the measurements and nearby regions. Atmospheric CO_2 concentration in the beginning of 1982 is assumed to be well-mixed and the corresponding simulated atmospheric mixing ratio is provided to the transport model for initialization.

C_a and $\delta^{13}C_a$ are regulated by two-way exchange of CO_2 and $^{13}CO_2$ from and to the ocean and land surface. Net transfer rates are determined by difference of these gross fluxes to yield atmosphere-to-surface net fluxes of carbon ($F_{as,net}$) and their corresponding signatures ($\delta^{13}C_{as,net}$).

To obtain $\delta^{13}C_a$ at the location of measurement stations, the transport model is run a second time over the same time period (1982 to 2012) with the gridded signature-

weighted net atmosphere-to-surface fluxes:

$$\delta^{13}F_{as,net}(\vec{\mathbf{x}},t) = F_{as,net}(\vec{\mathbf{x}},t) \cdot \delta^{13}\mathrm{C}_{as,net}(\vec{\mathbf{x}},t), \tag{1}$$

where $\delta^{13}F_{as,net}$ is the net atmosphere-to-surface δ^{13}C flux, e.g., in units of mol permil m^{-2} yr^{-1}. $\vec{\mathbf{x}}$ indicates location and t time; these indices are omitted in the following for brevity. $\delta^{13}\mathrm{C}_{as,net}$ is computed by dividing local $\delta^{13}F_{as,net}$ by local $F_{as,net}$.

This method of transporting signature-weighted net fluxes was chosen instead of separately transporting $^{13}CO_2$ and $^{12}CO_2$. Both approaches were tested and showed very similar results, with the exception of numerical issues in months having very small local $^{12}CO_2$ anomalies for the second approach.

Ocean, land, and fossil fluxes from the standard simulation are transported separately to quantify the contributions of these individual components to the simulated concentrations and signatures. For the sensitivity simulations $\mathbf{E}_{\mathrm{control}}$ and $\mathbf{E}_{\mathrm{noFF}}$ fossil fuel fluxes are not transported, consistent with the model setup.

The seasonal cycles of C_a and $\delta^{13}\mathrm{C}_a$ from TM3 are compared to observations. In the following, we focus on 3 out of the 19 available transport sites: Alert (82.5°N, Canada), Mauna Loa (19.5°N, Hawaii), and South Pole (90°S, Antarctica). Results for the other sites are shown in the supplementary. The Cooperative Global Atmospheric Data Integration Project (2013) product is used to compare atmospheric CO_2 at the simulation sites. For $\delta^{13}\mathrm{C}_a$ the SCRIPPS (Keeling et al., 2001) records for Alert, Mauna Loa and the South Pole are used. These records span a longer time period than the available transport matrices. For the remaining 16 sites, the shorter (1994 to 2009) records of GLOBALVIEW-CO2C13 (2009) are used.

The seasonal cycles are computed from observations and the TM3 results using the following procedure for either C_a or $\delta^{13}\mathrm{C}_a$, respectively. Months with missing values in either the observation or the TM3 simulation are masked in the TM3 and observational time series. Then the time series are detrended using a 12-month rolling mean and the overall mean of the series is set to zero. Finally, the mean for each calendar month is computed by averaging over all corresponding monthly values. Additionally, the standard deviation is computed for each calendar month to inform about the interannual variability of the seasonality.

2.3 The influence of carbon and isotope fluxes on the seasonal cycles of CO_2 and $\delta^{13}CO_2$

For diagnostic purposes, we analyze the carbon and isotope fluxes for their influence on the seasonal cycles of C_a and $\delta^{13}C_a$. We consider the atmosphere to be well mixed; the atmospheric transport operator is linear and the findings may qualitatively also apply to spatially-resolved fluxes. The budgets for the atmospheric inventories of CO_2 and $^{13}CO_2$ are:

$$\frac{d}{dt}N_a = -F^g_{as,net} \tag{2}$$

$$\frac{d}{dt}(N_a \cdot \delta^{13}C_a) = \left(\frac{d}{dt}N_a\right) \cdot \delta^{13}C_a + N_a \cdot \left(\frac{d}{dt}\delta^{13}C_a\right) = -F^g_{as,net} \cdot \delta^{13}C^g_{as,net} \tag{3}$$

N_a is the atmospheric carbon inventory and $F^g_{as,net}$ the globally integrated (superscript g) net atmosphere-to-surface carbon flux. We set $N_a = c{\cdot}C_a$, where c is a unit conversion factor (2.12 GtC/ppm). Solving for the change in C_a and $\delta^{13}C_a$ yields:

$$\frac{d}{dt}C_a = -\frac{1}{c} \cdot F^g_{as,net} \tag{4}$$

$$\frac{d}{dt}\delta^{13}C_a = \frac{1}{c \cdot C_a} \cdot \delta^{13}F^{g*}_{as,net}, \tag{5}$$

with

$$\delta^{13}F^*_{as,net} = F_{as,net} \cdot \left(\delta^{13}C_{as,net} - \delta^{13}C_a\right) \tag{6}$$

Eq. 6 corresponds to Eq. 1 for the net atmosphere-to-surface isotopic flux but is now referenced to the atmospheric signature instead the signature of 0 permil of the Vienna Pee Dee Belemnite standard as in Eq. 1.

Eq. 5 provides important insight. First, changes in $\delta^{13}C_a$ and, by interference, of its seasonal cycle are driven by $\delta^{13}F^*_{as,net}$. Negative values of $\delta^{13}F^*_{as,net}$ yield an increase in $\delta^{13}C_a$ and positive values a decrease. Typically, seasonal anomalies of $\delta^{13}F^*_{as,net}$ over land are negative over the growing season and positive otherwise, thereby, causing a seasonal cycle in $\delta^{13}C_a$. Changes in C_a, the denominator in Eq. 5, are relatively small over an individual season and can be considered constant within a given year. Second, the background CO_2 mixing ratio, C_a, modulates the magnitude of the $\delta^{13}C_a$ seasonal cycle. The seasonal cycle amplitude of $\delta^{13}C_a$ would be smaller under low preindustrial CO_2 than under modern CO_2 for equal seasonal variations in $\delta^{13}F^*_{as,net}$. Correspondingly, the seasonal cycle amplitude of $\delta^{13}C_a$ does not change as long as percentage changes in the

seasonal amplitude of $\delta^{13}F^*_{as,net}$ and in CO_2 are equal. We recall that the above equations and conclusions were derived by assuming a well-mixed atmosphere, while in reality spatial flux patterns and transport and their changes influence seasonal cycles at individual atmospheric stations.

2.4 Decomposition of $\delta^{13}F^*_{as,net}$

Next, we reformulate the net isotope flux in terms of net and gross carbon fluxes, isotopic discrimination, and isotopic disequilibrium (e.g., Mook (1986); Joos and Bruno (1998)) to diagnose their influence on the seasonal cycles.

The kinetic discrimination for a gross flux, e.g., from the atmosphere to the surface, is:

$$\varepsilon_{as} = (\delta^{13}\mathrm{C}_{as} - \delta^{13}\mathrm{C}_a), \tag{7}$$

with $\delta^{13}\mathrm{C}_{as}$ the signature of the gross flux from a to s (F_{as}) and $\delta^{13}\mathrm{C}_a$ the signature of the source. The isotopic disequilibrium (or difference) between atmosphere-surface gross fluxes is:

$$\delta_{dis,sa} = -\delta_{dis,as} = \left(\delta^{13}\mathrm{C}_{sa} - \delta^{13}\mathrm{C}_{as}\right) \tag{8}$$

The net carbon and isotope fluxes are differences between gross fluxes:

$$F_{as,net} = F_{as} - F_{sa} \tag{9}$$

$$\delta^{13}F^*_{as,net} = F_{as} \cdot \left(\delta^{13}\mathrm{C}_{as} - \delta^{13}\mathrm{C}_a\right) - F_{sa} \cdot \left(\delta^{13}\mathrm{C}_{sa} - \delta^{13}\mathrm{C}_a\right) \tag{10}$$

Rearranging yields:

$$\delta^{13}F^*_{as,net} = F_{as,net} \cdot \underbrace{\left(\delta^{13}\mathrm{C}_{as} - \delta^{13}\mathrm{C}_a\right)}_{\varepsilon_{as}} - F_{sa} \cdot \underbrace{\left(\delta^{13}\mathrm{C}_{sa} - \delta^{13}\mathrm{C}_{as}\right)}_{\delta_{dis,sa}} \tag{11}$$

The atmosphere-ocean gross carbon fluxes are given by the product of the air-sea gas transfer piston velocity and the fugacity of CO_2 in air and in sea water, respectively. For the land biosphere (index l), it follows from Eqs. 9 and 11:

$$F_{al,net} = \mathrm{NPP} - R \tag{12}$$

$$\delta^{13}F^*_{al,net} = F_{al,net} \cdot \varepsilon_{\mathrm{NPP}} \; - \; R \cdot \delta_{dis}, \tag{13}$$

with:

$$\delta_{dis} = \delta^{13}\mathrm{C}_R - \delta^{13}\mathrm{C}_{\mathrm{NPP}} \tag{14}$$

NPP is the net primary productivity of all plants within a grid cell. R is the sum of all release fluxes to the atmosphere, such as those from heterotrophic respiration, fire, mortality, and product pools. $\delta^{13}\mathrm{C}_R$ is the signature of R and $\delta^{13}\mathrm{C}_{NPP}$ is the signature of NPP, with $\varepsilon_{\mathrm{NPP}}$ (or ε_{al}) representing the (flux-weighted) fractionation by NPP. Here, as in LPX-Bern, we have assumed that the uptake difference between gross primary production (GPP) and NPP is released on short time scales and without further carbon isotope discrimination.

We turn to the calculation of the seasonal amplitude of $\delta^{13}F^*_{al,net}$ and its components. The time series of $\delta^{13}F^*_{al,net}$ is detrended by subtracting the trend (calculated with a rolling 12 months mean) and setting the mean to 0. Δ_{trend} is the difference between $\delta^{13}F^*_{al,net}$ after and before detrending. We define a seasonal mask to compute seasonal amplitudes of fluxes and their signatures. For each model year, we identify months in which detrended $\delta^{13}F^*_{al,net}$ is negative or equal to zero (roughly corresponding to the growing season). The sum of fluxes of these months is then termed the "seasonal amplitude" in a given year. For $\delta^{13}F^*_{al,net}$, this procedure is consistent with considering the difference between maximum and minimum values of the detrended cumulative sum of $\delta^{13}F^*_{al,net}$. Accordingly, the seasonal amplitudes of the component isotope and carbon fluxes contributing to $\delta^{13}F^*_{al,net}$ (Eq. 13; (NPP$-R$)$\cdot\varepsilon_{\mathrm{NPP}}$, $R\cdot\delta_{dis}$, and Δ_{trend}; (NPP-R), NPP, and R) are computed by summation over months where $\delta^{13}F^*_{al,net}$ is less or equal to zero within a given year. These component fluxes are not detrended to readily calculate the signatures δ_{dis} and ε_{NPP} by division of the seasonal amplitude isotopic flux with the corresponding seasonal amplitude carbon flux.

We note that the climatological mean values of the isotopic disequilibrium (δ_{dis}) the net carbon flux ($F_{al,net}$), and the net isotopic flux ($\delta^{13}F^*_{al,net}$) vanish by definition for the preindustrial equilibrium. However, this does not hold for their seasonal amplitudes. Further, the transport operations are linear. Thus, the contribution of the component fluxes of $\delta^{13}F^*_{al,net}$ ($F_{al,net}\cdot\varepsilon_{\mathrm{NPP}}$, $R\cdot\delta_{dis}$) to the seasonal cycle of $\delta^{13}\mathrm{C}_a$ are comparable, at least at the individual grid cell. Finally, detrending $\delta^{13}F^*_{al,net}$ before the computation of its seasonal amplitude is conistent with the calculation of the C_a and $\delta^{13}\mathrm{C}_a$ seasonal amplitude from the detrended atmospheric time series.

The comparison of Eqs. 12 and 13, together with Eqs. 4 and 5, provides insight. Putting the ocean aside, the seasonal cycle of C_a is driven by the spatio-temporal pattern of $F_{al,net}$, whereas the seasonal cycle of $\delta^{13}C_a$ is additionally influenced by seasonal variations in $\varepsilon_{\mathrm{NPP}}$, R, and δ_{dis}. Correspondingly, not only the seasonal signal of $F_{al,net}$, but also of the gross carbon exchange fluxes (NPP $\simeq R$), the transit time of assimilated carbon through the biosphere, co-controlling δ_{dis}, and isotopic discrimination should be represented well in models targeted to simulate the $\delta^{13}C_a$ seasonality. We conclude that the seasonal signal of $\delta^{13}C_a$ is influenced by different processes compared to the seasonal signal of C_a. This also applies to interannual variability and decadal-scale growth of seasonal amplitudes.

3 Results

3.1 Simulated spatial fluxes

The land biosphere shows a large seasonal signal in the net exchange of CO_2 with the atmosphere (Figure 1, panels (a,c,e). The northern extratropics show a net uptake of CO_2 during the Northern Hemispheric (NH) summer (June, July, and August (JJA)). In the NH winter (December, January, February (DJF)), these regions release CO_2 to the atmosphere. A similar seasonality is simulated in the northern tropical areas, with net CO_2 uptake during JJA explained by the presence of the tropical rain belt. In DJF, the tropical rain belt is shifted southwards and causes a dry season in the northern tropical areas, reducing production and leading to a net loss of CO_2 to the atmosphere. This seasonality pattern is mirrored over land in the Southern Hemisphere (SH).

Over the ocean, the net atmosphere-to-surface fluxes per area are generally much smaller than over land. Correspondingly, the seasonal net flux differences are smaller over the ocean than over land and the atmospheric CO_2 seasonal cycle is generally dominated by exchange with the land biosphere.

Turning to isotope fluxes (Figure 1, panels (b,d,f)), negative values of $\delta^{13}F^*_{as,net}$ cause an increase in $\delta^{13}C_a$ and positive fluxes a decrease (see section 2.3). During JJA negative $\delta^{13}F^*_{as,net}$ is simulated over NH land, increasing $\delta^{13}C_a$. This is expected, because atmosphere-to-land fluxes are dominated by photosynthesis during summer, which favours the incorporation of the lighter ^{12}C, leaving the atmosphere enriched in $^{13}CO_2$. During DJF isotopically depleted carbon is respired back to the atmosphere, overall de-

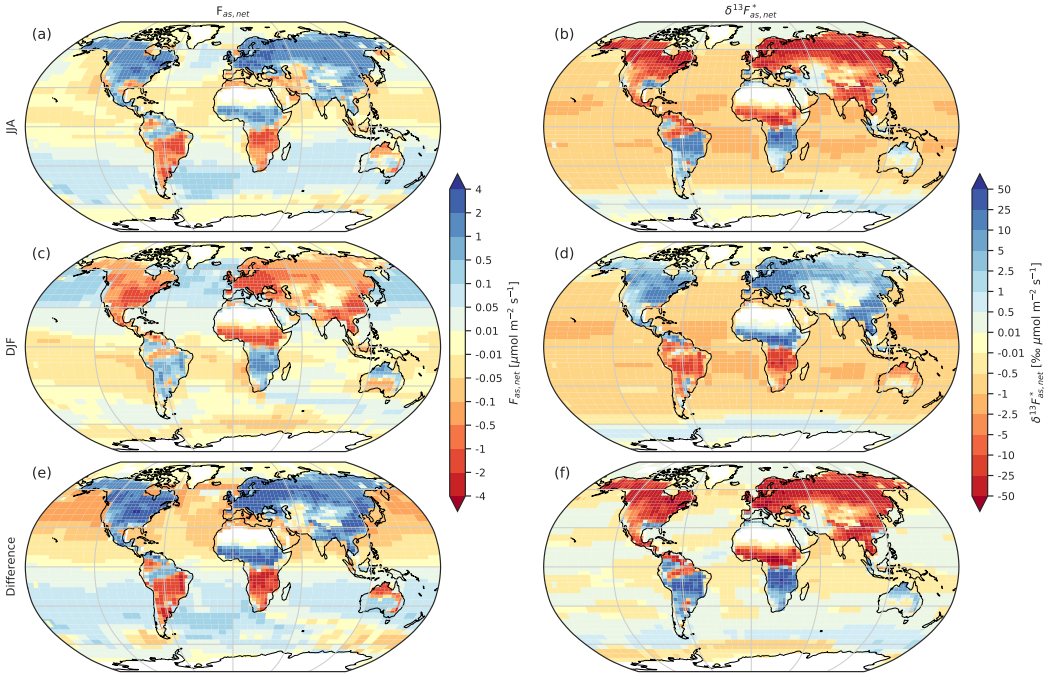

Figure 1. Net seasonal atmosphere-to-surface fluxes, averaged between 1982-2012 and for the standard setup ($E_{standard}$). The left panels (a,c,e) show the net CO_2 flux $F_{as,net}$, as simulated by Bern3D-LPX. The right panels (b,d,f) show the signature-weighted atmosphere-to-surface CO_2 flux $\delta^{13}F^*_{as,net}$ (see section 2.3). Negative (positive) values of $\delta^{13}F^*_{as,net}$ correspond to an expected increase (decrease) in $\delta^{13}C_a$. The top panels (a,b) show the fluxes averaged over the months of June, July, and August (JJA) and the middle panels (c,d) over December, January, and February (DJF). The bottom panels (e,f) show the difference between JJA and DJF. Note non-linear color bars and inverted colorscale in (b,d,f) versus (a,c,e), with blue colors in panels a to d indicating a lowering in atmospheric CO_2 and $\delta^{13}C$, respectively.

creasing $\delta^{13}C_a$. The SH terrestrial biosphere exhibits the same effect, but with inverted seasonality.

The ocean shows less spatial variability and generally weaker magnitudes in $\delta^{13}F^*_{as,net}$ than the land and a small seasonal cycle in $\delta^{13}F^*_{as,net}$. In both seasons, the ocean shows a negative $\delta^{13}F^*_{as,net}$ in low and mid latitudes, small modern fluxes in the northern subpolar gyres, and a positive flux in the Southern Ocean.

These modern Bern3D fluxes are driven by the atmosphere-ocean isotopic disequilibrium ($\delta_{dis,as}$; Eq. 8), with a negative $\delta_{dis,as}$ in low and mid latitudes, a small modern disequilibrium in northern high latitudes, and a positive $\delta_{dis,as}$ south of 50^oS, consistent with observations (Menviel et al., 2015; Quay et al., 2017; Becker et al., 2018).

The preindustrial atmosphere-ocean isotopic disequilibrium and net atmosphere-to-ocean isotopic flux are negative in low- and mid-latitude and positive in high-latitude regions. This pattern is mainly driven by the temperature dependency of isotopic discrimination during air-sea exchange and the cycling of marine biological matter (see Figure 1 of Menviel et al. (2015) for a comparison of Bern3D and LOVECLIM results for the atmosphere-ocean disequilibrium). The Suess effect causes a negative flux perturbation worldwide, shifting the net isotopic fluxes to more negative values over the industrial period (red colors in Figure 1).

3.2 Seasonal cycles of C_a and $\delta^{13}C_a$

Figure 2 compares the mean seasonal cycles of C_a and $\delta^{13}C_a$ with measurements from 1982 (Alert: 1985) to 2012 at three stations. Results from factorial transport simulations, where only the fluxes of land (green dashed line), the ocean (blue dashed line), and fossil fuel emissions (brown dashed lines) were considered are displayed as well.

For the northern station of Alert (panel (a)), both the timing and amplitude of the seasonal cycle of C_a are captured reasonably well in the model. The site is dominated by the NH terrestrial biosphere which shows a net uptake of carbon during NH summer months and a release during winter. There is only a minor contribution from ocean fluxes and fossil fuel emissions. The simulated amplitude in Alert is slightly overestimated (17.3 ppm) compared to the observations (14.8 ppm) and mean inter-annual variability is similar (0.84 ppm for the simulation vs 0.75 ppm for the observation). The seasonal cycle

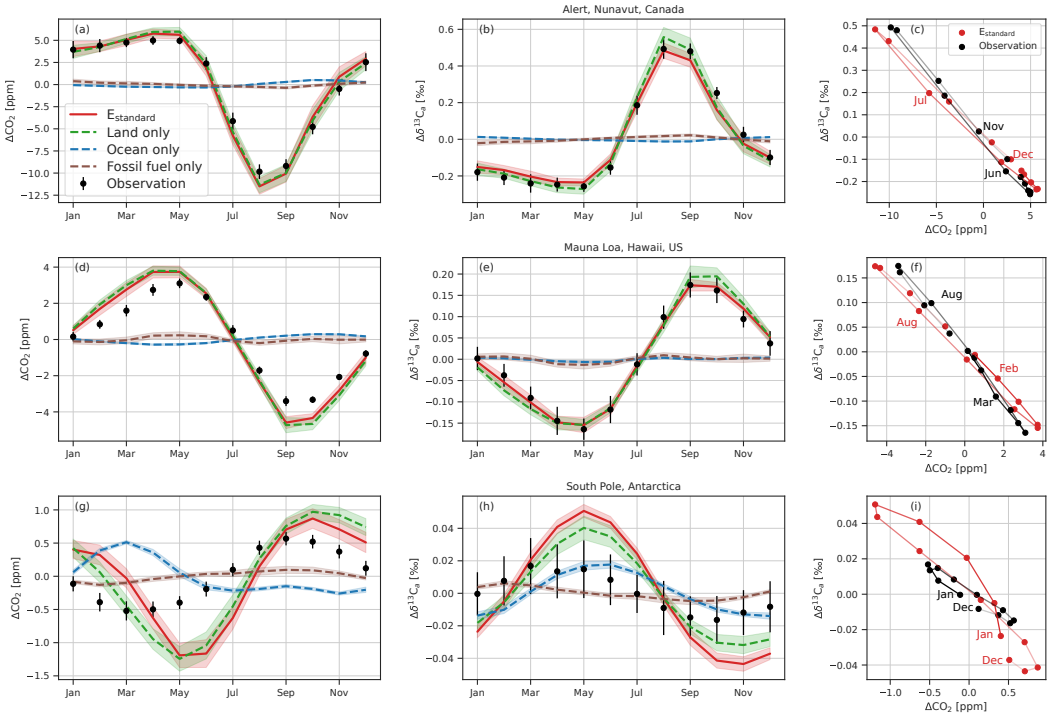

Figure 2. The simulated (red) seasonal cycle of atmospheric CO_2 (left (a,d,g)) and its signature $\delta^{13}C_a$ (middle (b,e,h)), compared to observations (black dots). Simulated values are from transporting net fluxes of the Bern3D-LPX standard simulation ($E_{standard}$) in TM3. The results for three measurement stations are shown: Top panels: Alert, northern Canada (a,b); middle panels: Mauna Loa, Hawaii (c,d); bottom panels: South Pole (e,f). The calculation of the seasonal cycle only considers months between 1982 and 2012 where both the measurements and transport matrices are available. The results of only transporting fluxes of terrestrial (green, dashed), oceanic (blue, dashed), and from fossil sources (brown, dashed) of the Bern3D-LPX standard simulation are shown with dashed lines. Error bars and shading correspond to the interannual standard deviation. In the rightmost panels (c,f,i) the seasonal anomalies (Δ) of CO_2 are plotted against those of $\delta^{13}C_a$. The lines connecting the monthly values fade with time throughout the year, i.e. the line connecting November to December is most transparent and selected months are labeled.

of $\delta^{13}C_a$ is also captured well in the model. Again, the signal is heavily dominated by the NH terrestrial biosphere, which releases isotopically-depleted carbon during winter and discriminates heavy ^{13}C during photosynthesis in the summer. The simulated amplitude (0.72 ‰) matches the observed amplitude (0.75 ‰) very well. Note that in contrast to the seasonality of C_a, the seasonality of $\delta^{13}C_a$ does not linearly decompose into the contributions of land, ocean, and fossil fuel emissions. A good model-data agreement in the phasing of the seasonal cycle of C_a relative to $\delta^{13}C_a$ is demonstrated The good agreement of the seasonal cycle in both CO_2 and $\delta^{13}C_a$ is also reflected in the scatter plot in panel (c). Both observation and model show a hysteresis behavior throughout the year, with the loop rotating in a clockwise direction. The hysteresis arises as the ratio between the rate of change in $\delta^{13}C_a$ versus the rate of change in C_a varies over the year (Heimann et al., 1989). This non-linearity in the atmospheric tracer relationship may arise from seasonally varying transport in combination with spatially and/or temporally varying relationships of atmosphere-surface $\delta^{13}C$ to CO_2 flux.

A similar picture is found at the Mauna Loa station in the tropical Pacific (Panels (c,d)). While the site is still dominated by NH land ecosystems, the overall amplitude is smaller for both C_a and $\delta^{13}C_a$. The model overestimates the seasonal amplitude of CO_2 (8.3 ppm vs 6.5 ppm) and has more interannual variability in simulation (0.3 ppm) than observation (0.24 ppm). On the other hand, the seasonal cycle of $\delta^{13}C_a$ is matched very well. The observed $\delta^{13}C_a$ amplitude (0.33 ‰) is almost identical to the amplitude of the observation (0.34 ‰) and the timing is also captured well. However, the mean standard deviation in the simulation is much smaller (0.013 ‰) compared to the observation (0.028 ‰). The rotation direction of the hysteresis loop is clockwise in the simulation, but anticlockwise in the observation (panel (f)). However, the observed hysteresis effect is small with offsets of less than 0.03 ‰.

Results for the South Pole show a different behavior (Panels (e,f)). Both the timing and amplitude of C_a (2.1 ppm simulated vs 1.1 ppm observed) do not agree. The absolute amplitude of observed C_a at the South Pole is over 10 times smaller than at Alert, and the absolute mismatch is therefore not as drastic as the relative mismatch. This remote site shows an expected relative larger dependence on the ocean. The C_a seasonality resulting from model ocean fluxes is partly opposite and shifted to that from the SH terrestrial biosphere. A mismatch is also apparent in the seasonal cycle of $\delta^{13}C_a$. The model overestimates the seasonal amplitude (0.094 ‰ vs 0.033 ‰). The observed am-

plitude at the South Pole is over 20 times smaller than at Alert. In contrast to the contribution to the seasonal cycle of C_a, the ocean shows a similar seasonality as the SH terrestrial biosphere, with high values during NH Winter and low values during summer. Observed interannual variability is significantly larger than simulated (0.015 ‰ vs 0.004 ‰). The disagreement between simulation and observation is also apparent when considering the scatter plot in panel (i). The model shows a complex hysteresis relationship, whereas the observation displays a clockwise loop.

3.3 Amplitude growth and the influence of fossil and land use emissions and climate change

The sensitivity of the seasonal cycle of C_a and $\delta^{13}C_a$ to different forcings is explored with sensitivity simulations. First, we compare modelled globally-averaged C_a and $\delta^{13}C_a$ with the observation-based records (Figure 3). The C_a evolution of the run with all forcings active ($E_{standard}$, red line panel (a)) captures the observed in broad terms (black dots). From 1700 to 1960 the model underestimates the atmospheric CO_2 increase. The discrepancy changes sign after 1960 and in 2020 the mean simulated mixing ratio is 420 ppm versus the observed 412 ppm. The $\delta^{13}C_a$ trend is matched relatively well until 1900 (Panel (b)), however, the simulation and observation diverge between 1900 and 1960, with the model showing a stronger decrease in signature. Between 1982 to 2010 (period for the transport model) the offset corrected trend matches the observation (inset panel (b)). At the end of the simulation in 2020, simulated atmospheric $\delta^{13}C_a$ is -9.1 ‰ compared to the observed -8.4 ‰.

The preindustrial control simulation $E_{control}$ simulates stationary C_a and $\delta^{13}C_a$ (Figure 3, dashed cyan line). $E_{constclim}$ produces results close to $E_{standard}$, ending with a lower C_a (412 vs 420 ppm). The difference in C_a is likely explained by a larger land sink without the effect of climate change. $E_{constclim}$ has a very minor effect on $\delta^{13}C_a$. The simulation without transient land use change (E_{noLU}) features a slower increase in C_a (389 ppm in 2020). The decrease of $\delta^{13}C_a$ is also slowed(-8.5 ‰), coincidentally matching the observation better in the latter half of the 20th century than the standard simulation. From 1982 to 2010 the constant land use simulation (E_{noLU}) shows almost an identical trend as $E_{standard}$. Besides E_{ctrl}, the simulation with no anthropogenic fossil fuel emissions (E_{noFF}) shows the largest difference from the standard run , reaching 306 ppm and -7 ‰in 2020. Almost all of the decrease in $\delta^{13}C_a$ takes place before 1970 in E_{noFF}. These

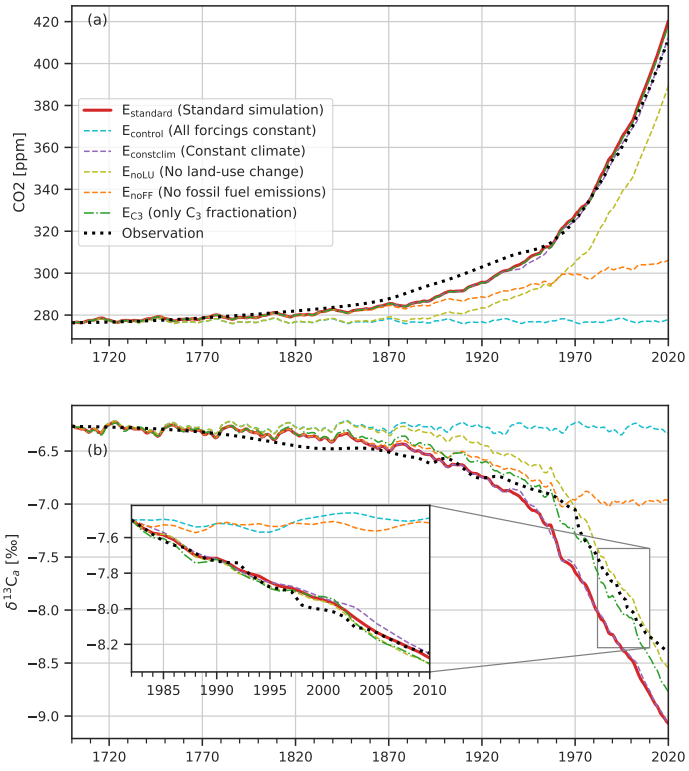

Figure 3. Global atmospheric CO_2 (top panel (a)) and $\delta^{13}C_a$ (bottom panel (b)) as simulated by Bern3D-LPX (red) compared to the observational records (black, dotted; (Friedlingstein et al., 2020; Graven et al., 2017)) for the period 1700-2020. $E_{control}$ (cyan, dashed) shows the results of a control simulation in which external forcings were kept constant (The fluctuations are caused by the inter-annual variability of the base-climate prescribed to the land model). $E_{constclim}$ (purple, dashed) corresponds to a simulation with unchanging climate, but with fossil emissions and land use. In E_{noLU} (olive, dashed) anthropogenic land use was kept constant at pre-industrial levels. Fossil-fuel emissions were disabled for the simulation E_{noFF} (orange, dashed). In addition to the factorial forcing simulations a simulation where all plants use C3 photosynthetic discrimination (E_{C3}) is displayed (green, dot-dashed). The inset in panel (b) shows a zoomed in view of the transport period 1982 - 2012. In the inset values from the simulations are shifted to match the atmospheric $\delta^{13}C_a$ in the year 1982.

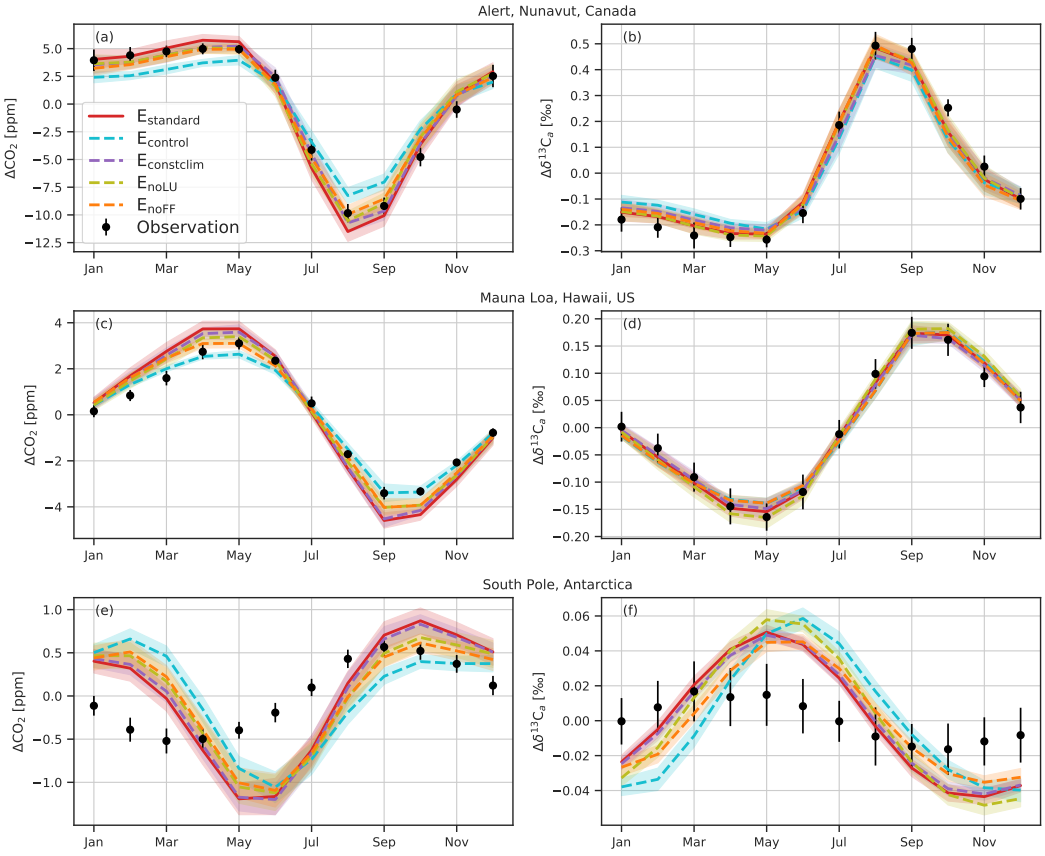

Figure 4. The seasonal cycle of CO_2 (left panels; (a,c,e)) and $\delta^{13}C_a$ (right panels; (b,d,f)) at Alert, northern Canada (a,b), Mauna Loa, Hawaii (c,d) and South Pole (e,f) as simulated by Bern3D-LPX and transported with TM3 (red), compared to observations (black dots). The calculation of the seasonal cycle only considers months between 1982 and 2012 where both the measurements and transport matrices are available. The results of sensitivity simulations are shown with dashed lines: $E_{control}$ (cyan,dashed), $E_{constclim}$ (purple, dashed), E_{noLU} (olive, dashed) and E_{noFF} (orange, dashed). Shading and error bars correspond to the interannual standard deviation.

results highlight the dominant role of fossil fuel emissions for the C_a and $\delta^{13}C_a$ trends over the historical period.

In Figure 4 the response of the seasonal cycle in C_a and $\delta^{13}C_a$ to the sensitivity experiments is shown. The change between $E_{control}$ and $E_{standard}$ (dashed blue versus red lines) reveals the change in seasonal amplitudes over the industrial period. For C_a, a growth in amplitude is clearly visible (12.2 ppm to 17.25 ppm at Alert; 6 ppm to 8.3

ppm at Mauna Loa; 1.7 to 2.1 ppm at the South Pole). Across all 19 sites the amplitude in C_a has grown by 44% ± 35% (mean ± standard deviation) from 1700 AD to (1982-2010).

For $\delta^{13}C_a$, the control simulation exhibits an almost identical amplitude averaged across all 19 sites (2% ± 16% lower in $E_{control}$ than $E_{standard}$). Larger deviations at individual sites than on average are apparent in Figure 4, where a moderately smaller amplitude in $E_{control}$ is visible in Alert, almost identical results are found at Mauna Loa and a slightly higher amplitude is found at the South Pole in the control. The changes are in general small at the NH stations, whereas more diverse results are simulated at the SH stations with both smaller or larger amplitudes in the control than in the standard (SI Figure S4).

Fossil fuel emission, land use change, and climate change contribute to the seasonal amplitude changes. For C_a, the exclusion of fossil fuel emission (E_{noFF}) results in a mean amplitude reduction of 19% ± 12% compared to $E_{standard}$. E_{noLU} produces amplitudes that are 9% ± 4% smaller on average than $E_{standard}$. $E_{constclim}$ has the smallest impact on the seasonal amplitude of C_a, with the amplitude being on average 3% ± 4% smaller than in $E_{standard}$.

For $\delta^{13}C_a$, E_{noFF} exhibits on average a 9% ± 14% smaller amplitude than $E_{standard}$, a larger deviation than for $E_{control}$. E_{noLU} on the other hand, increases the amplitude compared to $E_{standard}$ by 10% ± 8% on average. The effect of $E_{constclim}$ is only minor with the amplitude being 3% ± 3% smaller on average.

In summary, we simulated a growth in the C_a seasonal amplitudes over the historical period, but little change in the $\delta^{13}C_a$ seasonal amplitude at NH sites (red vs blue lines in Figure 4 and Supplementary Figure S4). The growth in C_a seasonal amplitude is mainly forced by raising CO_2 from fossil-fuel and land use emissions, while the contribution from climate change is small.

3.4 Zonal decomposition of land-biosphere fluxes

In panel (a) of Figure 5 the seasonal amplitude of the signature-weighted, detrended land fluxes $\delta^{13}F^*_{al,net}$ is shown averaged zonally for $E_{standard}$ (thick red line) and $E_{control}$ (dashed red line). In $E_{standard}$ the northern mid to high latitude ecosystem fluxes exhibit

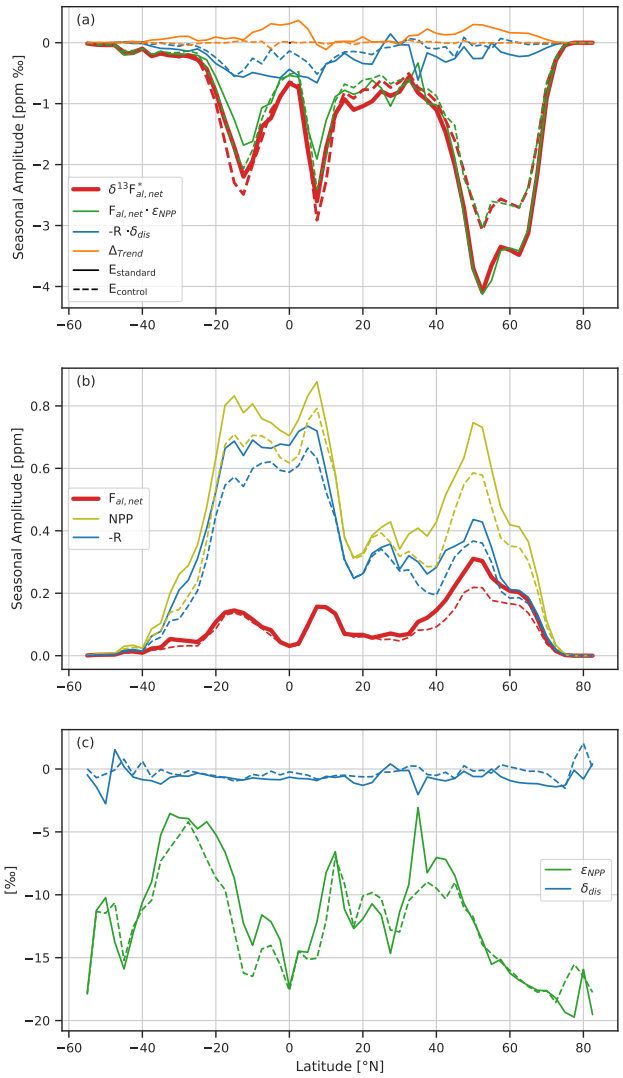

Figure 5. The seasonal amplitude per 2.5° latitude band of the signature-weighted, detrended net atmosphere-land flux $\delta^{13}F^*_{al,net}$ in the time period 1982-2012 is shown in panel (a) in red. This quantity is the sum of three constituents seasonal amplitudes (section 2.4): Net land-atmosphere flux weighted with photosynthetic discrimination ($F_{al,net} \cdot \varepsilon_{NPP}$, green) plus release fluxes weighted with the disequilibrium signature (-$R \cdot \delta_{dis}$, blue) plus the contribution to the seasonal amplitude by the underlying trend of $\delta^{13}F^*_{al,net}$ (Δ_{trend}, orange) (sign convention: "green+blue+orange=red"). The results from the standard simulation ($E_{standard}$, solid lines) are compared to the control simulation ($E_{control}$, dashed lines). In panel (b), the seasonal amplitudes of (non-detrended) net carbon fluxes are shown. The net atmosphere-land flux ($F_{al,net}$ (red) is split in Net Primary Productivity (NPP, olive) and release flux (R, blue). In the bottom panel (c) the corresponding discrimination of photosynthesis ε_{NPP} and the disequilibrium signature δ_{dis} is shown. All values are for the period with $\delta^{13}F^*_{al,net}$ smaller than zero ($\sim$ growing season).

the strongest seasonal cycle (solid red line), followed by tropical rain green ecosystems. This pattern contributes to the larger seasonal amplitudes of $\delta^{13}C_a$ in the NH extratropics versus tropical and SH stations. The same pattern holds true for $E_{control}$, however the seasonal amplitude of the northern ecosystems (40°N to 70°N) is 1.29 larger for $E_{standard}$ than $E_{control}$, close to the observed increase in atmospheric CO_2 of 1.32 from pre-industrial to the reference period of 1982-2012. This is not the case in the tropical and SH ecosystems with $E_{control}$ sometimes exhibiting larger amplitudes than $E_{standard}$ Figure 5). The near proportional growth in the seasonal amplitude of $\delta^{13}F^*_{al,net}$ and mean atmospheric CO_2 in the NH likely explains the absence of a change in seasonal amplitude of $\delta^{13}C_a$ at NH stations (Eq. 5; see also Supplementary Figure S4).

Turning to CO_2, the seasonal amplitude of the modeled zonally-averaged net atmosphere-to-land CO_2 flux, $F_{al,net}$, shows largest values in the NH extratropics and a large increases over the historical period in the NH extratropics of 35% between 20° N to 70° N, a much smaller absolute increase in the SH extratropics, and little change in the tropics of 6% between -20° N to 20°N (Figure 5b, dashed vs solid red lines). This increase in seasonal amplitude of $F_{al,net}$ drives the increase in the CO_2 seasonal amplitudes. We emphasize that the growth of seasonal amplitude in flux should not be confused with the annual net land carbon sink.

The decomposition of the seasonal amplitude of $\delta^{13}F^*_{al,net}$ into constituent fluxes (see section 2.4) is displayed in panel (a) of Figure 5. A large part of the signal is explained by the net atmosphere-land flux ($F_{al,net}$) weighted with the signature of photosynthesis (ε_{NPP}) for both $E_{standard}$ and $E_{control}$. The disequilibrium flux ($-R{\cdot}\delta_{dis}$) has only a small contribution to the seasonal amplitude for northern mid to high latitude ecosystems for $E_{standard}$ and is almost negligible for $E_{control}$. The relative importance of $R{\cdot}\delta_{dis}$ is enhanced for the tropical dryland ecosystems, where a significant part of the seasonal amplitude of $\delta^{13}F^*_{al,net}$ is related to the disequilibrium flux. Note that in $E_{control}$, the disequilibrium flux albeit smaller than in $E_{standard}$ is not negligible. This is most likely caused by differences in respiration signatures due to the lagged response to natural changes in ε_{NPP}. The effect of Δ_{trend} is visible in $E_{standard}$: The removal of the trend leads to a reduction of the observed seasonal amplitude. As expected Δ_{trend} is close to zero in $E_{control}$.

The seasonal amplitude of net primary productivity and total release flux (R) increase not only in northern ecosystems but also in the tropics (Figure 5b). Note that the seasonal amplitudes of NPP and R are not close to zero for non-seasonal ecosystems. This is a consequence of the definition of the seasonal amplitude via the sign of $\delta^{13}F^*_{al,net}$, i.e. fluxes are evaluated roughly over the growing season. The zonal variation in (growing season) photosynthetic discrimination ε_{NPP} is mainly due to differences in vegetation composition, with the C4 plants having considerably lower fractionation (Figure 5c). In $\mathrm{E_{standard}}$ the discrimination is decreasing as compared to $\mathrm{E_{control}}$ which is consistent with the simulated increase in the prevalence of C4 plants. The disequilibrium signature δ_{dis} is closer to zero for the control than standard simulation. This is expected because the signal from the atmospheric Suess effect in R is delayed relative to NPP by vegetation, soil and product pool lifetimes, leading to a disequilibrium with respect to the production signature.

In summary, the seasonal amplitude of $\delta^{13}F^*_{al,net}$ increases roughly proportional to atmospheric CO_2 in the NH extratropics, likely explaining the absent trend in the seasonal amplitude of $\delta^{13}C_a$ at NH stations. Zonal and temporal variations in the seasonal amplitude of $\delta^{13}F^*_{al,net}$ are mainly driven by variations in the the isotopic signature of NPP and the net carbon flux over the growing season, with further contributions from isotopic disequilibria, and the long-term trend in $\delta^{13}F^*_{al,net}$.

4 Discussion

4.1 Atmosphere-surface fluxes in Bern3D-LPX

The large-scale atmosphere-ocean fluxes and seasonality simulated by the Bern3D model are broadly comparable to observational estimates over large parts of the ocean (Landschützer et al., 2014; Takahashi et al., 2009), with ocean CO_2 outgassing in the tropics and uptake in the mid-latitudes during winter. Model-data differences remain, in particular in the Southern Ocean and the subpolar gyres. Observation-based analyses indicate a stronger ocean CO_2 uptake in summer than in winter in the Southern Ocean (Landschützer et al., 2018; Long et al., 2021) and the northern subpolar gyres (Landschützer et al., 2018), in contrast to Bern3D results and more complex ocean models (Hauck & Völker, 2015) and several Earth System Models from CMIP5 (Majkut et al., 2014) and CMIP6 (unpublished analysis of CMIP6 model output; not shown). The coarse-resolution,

cost-efficient Bern3D model underestimates interannual variability in climate and carbon fluxes as El Nino-Southern Oscillation and other modes of variability are missing.

The regional patterns of atmosphere-land fluxes are an active area of research (Kondo et al., 2020; Bastos et al., 2020; Jung et al., 2020; Gaubert et al., 2019; Friedlingstein et al., 2020), and large uncertainties on the geographical distribution of fluxes persist. The performance of LPX-Bern with respect to various observational metrics is systematically assessed in Lienert and Joos (2018) and further explored in a range of studies (Seiler et al., 2022; Müller & Joos, 2021; Tschumi et al., 2021; Joos et al., 2020; Müller & Joos, 2020). The model is able to capture many metrics reasonably well, but is on the low end of the range of land carbon uptake. Interannual variability of global carbon fluxes simulated by LPX-Bern is similar, or even somewhat larger, in comparison with other models and observational estimates (Friedlingstein et al., 2020).

On the global scale, Bern3D-LPX combined with fossil fuel emission estimates is able to broadly reproduce the historic evolution of atmospheric CO_2 (Figure 3). The lower simulated concentration up to 1960, means that either the sink terms (land and ocean) are too big, or the emissions from land use change or prescribed fossil fuels are too small. Conversely, the too high concentration after 1960, would stem from the opposite effect. LPX-Bern is known to be biased low in land-sink and land use emissions (Lienert & Joos, 2018), which could explain the observed behaviour. Additionally, uncertainties of prescribed land use states and fossil fuel emissions, could also contribute to the mismatch.

The discrepancy in the simulated global $\delta^{13}C_a$ is large between 1900 and 1960, with the model showing a stronger decline in $\delta^{13}C_a$ than observed (Figure 3). After 1960, modeled and observed changes agree very well in the standard simulation (Figure 3, inset). It is hard to pinpoint the exact reasons for the mismatch. In addition to uncertainties in net carbon fluxes, the magnitude of gross exchange fluxes, overturning time scales, and accurate $\delta^{13}C$ signatures of the air-to-sea , air-to-land, and fossil fluxes are of importance. Discrimination in Bern3D-LPX is described following (Lloyd & Farquhar, 1994) and 20th century changes in the isotopic fractionation of C3 trees, and thus intrinsic water-use efficiency, simulated with LPX-Bern are found to be consistent with a global tree ring compilation (Keller et al., 2017). On the other hand, LPX-Bern simulates a too large coverage by C4 plants on natural land which expands under raising CO_2, thereby changing on average discrimination to less negative values($\Delta\varepsilon_{\mathrm{NPP}} \sim 1‰$; Supplementary Fig-

ure S6). This model bias likely contributes to the model-data mismatch in the historical $\delta^{13}C_a$ trend for the standard simulation (Figure 3). An additional sensitivity simulation (E_{C3}), with the discrimination formulation for all C4 plants replaced by those for C3 plants, shows indeed a small negative trend in globally-averaged discrimination (about 0.5 ‰; Supplementary Figure S6) and smaller deviations between modeled and observed $\delta^{13}C_a$ change (Figure 3).

The change in $\delta^{13}C_a$ in the period where fluxes are transported using the transport matrices (1982-2012), is reproduced well in the model (Figure 3). The transport model uses the simulated atmospheric CO_2 and $\delta^{13}C_a$ as a background in the first year of transport. To test the influence of the mismatch prior to the transport period, the transport was also executed using observed atmospheric CO_2 and $\delta^{13}C_a$, yielding near indistinguishable results for the seasonality of CO_2 and $\delta^{13}C_a$ (Figure S5).

4.2 Observed versus simulated mean seasonal cycles of C_a and $\delta^{13}C_a$

The amplitude of the mean seasonal cycle of atmospheric CO_2 (C_a) and its $\delta^{13}C$ signature ($\delta^{13}C_a$) is captured well by our model chain at Northern Hemisphere (NH) and near-equatorial (Christmas Island and Mahe Island) stations, though deviations remain (Figure 2 and Supplementary Figures S1 and S2). The seasonal amplitudes are much smaller in the Southern Hemisphere (SH) than NH, with observed amplitudes more than ten times larger for C_a and even more than twenty times larger for $\delta^{13}C$ at Alert than at the South Pole. The small amplitudes render the correct simulation of SH seasonality challenging. The seasonal amplitudes are overestimated in SH for both tracers and the bias in amplitude increases generally from low to high southern latitudes (Supplementary Figures S1 and S2). The terrestrial signal dominates simulated seasonality at all stations. Ocean and fossil fluxes have small impacts on seasonality in the NH but are relatively more important in the SH. Long et al. (2021) use atmospheric measurements and inverse models to show that the CO_2 seasonal cycle over the Southern Ocean is dominated by air-sea exchange, with little contribution from terrestrial and fossil carbon fluxes. This finding and our results suggest that the transport of the terrestrial and fossil signals to high southern latitudes is overestimated.

The C_a seasonal cycle resulting from atmosphere-ocean flux is smaller in amplitude and shifted in time by up to six months compared to observations at the three Antarc-

tic stations (Palmer, Halley, South Pole; blue lines versus black dots in Supplementary Figure S1). This model-data mismatch in amplitude and phase is likely caused by the biases in the Bern3D Southern Ocean CO_2 flux. In contrast, the simulated amplitude and phasing of the $\delta^{13}C_a$ seasonal cycle resulting from the ocean is well in line with observations at Palmer and Halley station (Supplementary Figure S2). This agreement suggests that the seasonality of the net atmosphere-ocean isotope flux over the Southern Ocean is reasonably well represented by Bern3D, in contrast to the seasonality of the net CO_2 flux. The different phasing in ocean-related C_a and $\delta^{13}C_a$ seasonality in the model is explained as follows. Seasonality of C_a is controlled by the net atmosphere-to-ocean CO_2 flux, while seasonality of $\delta^{13}C_a$ is primarily driven by the isotopic disequilibrium flux ($F_{a,s} \cdot \delta_{dis}$; Eq. 11) The air-sea gas exchange piston velocity, and, in turn, F_{as} and the disequilibrium flux are larger under high winds in winter than in summer in the model Southern Ocean, consistent with the observed seasonal phasing of $\delta^{13}C_a$ at the Antarctic stations.

The effect of external forcings on the seasonal cycle of $\delta^{13}C_a$ and C_a is explored using sensitivity simulations. The impact of land use and climate forcing on the mean $\delta^{13}C_a$ seasonality is generally small. The seasonal cycle of $\delta^{13}C_a$ is, in general, less sensitive than that of C_a to external forcing.

On a technical note,transporting simulated ^{13}C fluxes is not without challenges. The definition of the δ-notation can pose numerical difficulties when net ^{12}C fluxes are close to zero. We found that transporting signature-weighted total carbon fluxes to be the most reliable method for arriving at local $\delta^{13}C_a$. Similarly, seemingly small errors in the model representation of gross fluxes and mass balances, can become critical when considering net surface-to-atmosphere fluxes (See also section 2.1).

4.3 Growth in seasonal cycle amplitudes

The seasonal cycle amplitude of C_a is observed to grow over time pending on location (Bacastow et al., 1985; Barlow et al., 2015; Piao et al., 2018). In contrast, the observations from the (GLOBALVIEW-CO2C13, 2009) product do not show a consistent change of $\delta^{13}C_a$ seasonal amplitude. The observed amplification of the CO_2 seasonal cycle is captured by our model as discussed elsewhere (Lienert & Joos, 2018).

Modeled changes in the $\delta^{13}C_a$ seasonal amplitude yield no clear trend in the standard case over the simulation period 1982 to 2012, consistent with the observations. Similarly, $\delta^{13}C_a$ seasonal amplitudes are very similar for the preindustrial control and the standard case at the NH stations (dashed blue vs red line in Figure 4 and Supplementary Figure S4).

The absence of a trend in the seasonal cycle amplitude of $\delta^{13}C_a$ is expected for a concurrent growth in the seasonal signal of $\delta^{13}F^*_{as,net}$ and in atmospheric CO_2 of equal proportion (see section 2.3). Both the background CO_2 mixing ratio and the seasonal amplitude of $\delta^{13}F^*_{al,net}$ in NH temperate and boreal ecosystems (40°N to 70°N) increase by about 30% from preindustrial to modern (1982-2012) (difference between dashed and solid red lines in Figure 5). The seasonal signal of $\delta^{13}F^*_{al,net}$ is largest in this region and dominates NH $\delta^{13}C_a$ seasonality. The modeled seasonal signal of $\delta^{13}F^*_{al,net}$ shows little change or even decreases over the industrial period in tropical and SH ecosystems (Figure 5). This is partly reflected in a decrease in $\delta^{13}C_a$ seasonal amplitude from preindustrial to modern at Ascension and the Antarctic stations (Supplementary Figure S4). The simulated amplitude is dominated by the land contribution at these stations (Supplementary Figure S2). Regarding observations, the short record length does not permit to robustly identify any trends in $\delta^{13}C_a$ seasonal amplitude and model results for $\delta^{13}C_a$ seasonal amplitude growth are consistent with observations, within their uncertainties.

4.4 Seasonality: C_a versus $\delta^{13}C_a$

Observations of $\delta^{13}C_a$ seasonality may provide different, complementary information compared to observations of C_a seasonality. Our results and the theoretical considerations in section 2.3 and 2.4 partly support this notion. For example, the C_a seasonal amplitude is overestimated by our model at Mauna Loa, whereas simulated and observed $\delta^{13}C_a$ seasonal amplitude closely agree (Figure 2). Another example, is the phasing of the ocean-related seasonal cycles in the Southern Ocean region, discussed above.

The decomposition of $F_{al,net}$ and $\delta^{13}F^*_{al,net}$ into constituent fluxes (Figure 5) enables insights into the information contained in the seasonal cycle of $\delta^{13}C_a$. For land ecosystems, we find that most of the modeled seasonal signal can be explained by the net atmosphere-land flux weighted by the signature of photosynthesis. The contribution of respiration and decay processes, which emit old and light carbon to the atmosphere, is relatively small

for northern ecosystems. For tropical ecosystems this disequilibrium plays a larger role (blue versus green line in Figure 5a), pointing towards a potential role of seasonal observations of $\delta^{13}C_a$ in constraining fluxes in these ecosystems.

The analysis in section 2.3 and 2.4 (Eqs. 5 and 13) show that the seasonal signal of net carbon sink flux, discrimination during photosynthesis, isotopic disequilibrium, and the gross exchange flux between land biosphere and atmosphere (R) as well as their long-term trends and spatial patterns influence $\delta^{13}C_a$ seasonality at individual sites. Thus, several ecosystem processes are relevant to correctly simulate the seasonal cycle of $\delta^{13}C_a$. For example, seasonal variations and industrial-period trends in ε_{NPP} may be influenced by shifts between C3 and C4 plants due to climate and land use changes. Changes in intrinsic water use efficiency related to stomatal conductance of CO_2 and water may also affect ε_{NPP}. Disequilibrium fluxes ($R{\cdot}\delta_{dis}$) are expected to grow in response to the observation-inferred increase in NPP, which, in turn, affects R. Similarly, heterotrophic respiration, fire fluxes, and fluxes from deforestation and products, all contributing to R, are expected to change under warming and human land use. The disequilibrium δ_{dis} is a measure of the age of respired carbon relative to atmospheric carbon. δ_{dis} is growing in response to the Suess effect from growing fossil fuel (and land use) emissions. Mechanisms driving the current land carbon sink are still debated. We may expect different $\delta^{13}C_a$ seasonality if the global carbon sink is driven by a stimulation of NPP, e.g., by CO_2 fertilization, versus a change in tree longevity. These two mechanisms may affect the disequilibrium flux differently. It remains a future task, e.g., by applying perturbed parameter ensembles and sensitivity simulations, to investigate whether such differences indeed significantly affect $\delta^{13}C_a$ seasonality.

5 Conclusion

In conclusion, we explored the global-scale mechanisms driving the observed seasonal cycle of atmospheric $\delta^{13}C_a$ using atmosphere-surface fluxes from the Bern3D-LPX Earth System Model of Intermediate Complexity and fossil emissions in combination with transport matrices from the TM3 atmospheric transport model. The $\delta^{13}C$ seasonal cycle is strongly dominated by land biosphere carbon fluxes, in particular in the Northern Hemisphere and the tropics. The sensitivity of the $\delta^{13}C$ seasonal cycle to climate change and land use fluxes was found to be small over the period with atmospheric $\delta^{13}C$ data. Observations of the $\delta^{13}C$ seasonal cycle provide partly complementary information com-

pared to the CO_2 seasonal cycle. This suggest that the observed $\delta^{13}C_a$ seasonal cycle offers a novel constraint for land biosphere models used to simulate the terrestrial sink of anthropogenic carbon and land use emissions.

Appendix A Open Research

The data displayed in the figures will be made freely available at Zenodo or a similar site when the manuscript is accepted. For the review process the data and plotting scripts are available as a download: https://cloud.climate.unibe.ch/s/g9qrit7KDRnrbLp

Acknowledgments

This project has received funding from the European Union's Horizon 2020 research and innovation programme under grant agreement No 821003 (project 4C, Climate-Carbon Interactions in the Current Century) and by the Swiss National Science Foundation (project #200020_200511). The work reflects only the authors' view; the European Commission and their executive agency are not responsible for any use that may be made of the information the work contains. We thank the researchers of the Cooperative Atmospheric Data Integration Project, NOAA ESRL, Boulder, Colorado, and of the Scripps CO_2 program for making their CO_2 and $\delta^{13}C$ data freely available and Martin Heimann for suggesting to plot seasonal anomalies of CO_2 versus those of $\delta^{13}C$. A special thanks goes to Christoph Köstler for providing the TM3 transport matrices.

References

Andres, R., Boden, T., & Marland, G. (2009a). *Monthly Fossil-Fuel CO2 Emissions: Isomass of Emissions Gridded by One Degree Latitude by One Degree Longitude.* Carbon Dioxide Information Analysis Center (CDIAC), Oak Ridge National Laboratory (ORNL), Oak Ridge, TN (United States. doi: 10.3334/CDIAC/FFE.MONTHLYISOMASS.2016

Andres, R., Boden, T., & Marland, G. (2009b). *Monthly Fossil-Fuel CO2 Emissions: Mass of Emissions Gridded by One Degree Latitude by One Degree Longitude - 2016.* Carbon Dioxide Information Analysis Center (CDIAC), Oak Ridge National Laboratory (ORNL), Oak Ridge, TN (United States). doi: 10.3334/CDIAC/FFE.MONTHLYMASS.201

Andres, R., Boden, T., & Marland, G. (2017). *Annual Fossil-Fuel CO2 Emissions:*

Global Stable Carbon Isotopic Signature. CDIAC. doi: 10.3334/CDIAC/FFE .DB1013.2017

Andres, R., Marland, G., Boden, T., & Bischof, S. (2000). Carbon dioxide emissions from fossil fuel consumption and cement manufacture, 1751-1991, and an estimate of their isotopic composition and latitudinal distribution. In D. Schimmel (Ed.), *The carbon cycle* (pp. 53–62).

Bacastow, R. B., Keeling, C. D., & Whorf, T. P. (1985, 10). Seasonal amplitude increase in atmospheric CO2 concentration at Mauna Loa, Hawaii, 1959-1982. *Journal of Geophysical Research: Atmospheres*, *90*(D6), 10529–10540. doi: 10.1029/JD090iD06p10529

Ballantyne, A. P., Miller, J. B., & Tans, P. P. (2010). Apparent seasonal cycle in isotopic discrimination of carbon in the atmosphere and biosphere due to vapor pressure deficit. *Global Biogeochemical Cycles*, *24*(3), 1–16. doi: 10.1029/2009GB003623

Barlow, J. M., Palmer, P. I., Bruhwiler, L. M., & Tans, P. (2015). Analysis of CO2 mole fraction data: First evidence of large-scale changes in CO2 uptake at high northern latitudes. *Atmospheric Chemistry and Physics*, *15*(23), 13739–13758. doi: 10.5194/acp-15-13739-2015

Bastos, A., Ciais, P., Chevallier, F., Rödenbeck, C., Ballantyne, A. P., Maignan, F., ... Zhu, D. (2019). Contrasting effects of CO2 fertilization, land-use change and warming on seasonal amplitude of Northern Hemisphere CO2 exchange. *Atmospheric Chemistry and Physics*, *19*(19), 12361–12375. doi: 10.5194/acp-19-12361-2019

Bastos, A., O'Sullivan, M., Ciais, P., Makowski, D., Sitch, S., Friedlingstein, P., ... Zaehle, S. (2020, 2). Sources of Uncertainty in Regional and Global Terrestrial CO2 Exchange Estimates. *Global Biogeochemical Cycles*, *34*(2). doi: 10.1029/2019GB006393

Battaglia, G., & Joos, F. (2018). Marine N2O Emissions From Nitrification and Denitrification Constrained by Modern Observations and Projected in Multimillennial Global Warming Simulations. *Global Biogeochemical Cycles*, *32*(1), 92–121. doi: 10.1002/2017GB005671

Becker, M., Steinhoff, T., & Körtzinger, A. (2018, 9). A Detailed View on the Seasonality of Stable Carbon Isotopes Across the North Atlantic. *Global Biogeo-*

chemical Cycles, *32*(9), 1406–1419. doi: 10.1029/2018GB005905

Brüggemann, N., Gessler, A., Kayler, Z., Keel, S. G., Badeck, F., Barthel, M., ... Bahn, M. (2011). Carbon allocation and carbon isotope fluxes in the plant-soil-atmosphere continuum: A review. *Biogeosciences*, *8*(11), 3457–3489. doi: 10.5194/bg-8-3457-2011

Cooperative Global Atmospheric Data Integration Project. (2013). *Multi-laboratory compilation of synchronized and gap-filled atmospheric carbon dioxide records for the period 1979-2012 (obspack_co2_1_GLOBALVIEW-CO2_2013_v1.0.4_2013-12-23).* Compiled by NOAA Global Monitoring Division: Boulder, Colorado, U.S.A. doi: 10.3334/OBSPACK/1002

Dargaville, R. J., Heimann, M., McGuire, A. D., Prentice, I. C., Kicklighter, D. W., Joos, F., ... Wittenberg, U. (2002). Evaluation of terrestrial carbon cycle models with atmospheric CO2 measurements: Results from transient simulations considering increasing CO2, climate, and land-use effects. *Global Biogeochemical Cycles*, *16*(4). doi: 10.1029/2001gb001426

Evans, J. R., & Von Caemmerer, S. (2013). Temperature response of carbon isotope discrimination and mesophyll conductance in tobacco. *Plant, Cell and Environment*, *36*(4), 745–756. doi: 10.1111/j.1365-3040.2012.02591.x

Farquhar, G. (1983). On the Nature of Carbon Isotope Discrimination in C4 Species. *Functional Plant Biology*, *10*(2), 205. doi: 10.1071/PP9830205

Farquhar, G. (1989). Carbon Isotope Discrimination And Photosynthesis. *Annual Review of Plant Physiology and Plant Molecular Biology*, *40*(1), 503–537. doi: 10.1146/annurev.arplant.40.1.503

Farquhar, G., & Cernusak, L. (2012). Ternary effects on the gas exchange of isotopologues of carbon dioxide. *Plant, Cell and Environment*, *35*(7), 1221–1231. doi: 10.1111/j.1365-3040.2012.02484.x

Forkel, M., Carvalhais, N., Rödenbeck, C., Keeling, R., Heimann, M., Thonicke, K., ... Reichstein, M. (2016). Enhanced seasonal CO2 exchange caused by amplified plant productivity in northern ecosystems. *Science*, *351*(6274), 696–699. doi: 10.1126/science.aac4971

Friedlingstein, P., O'Sullivan, M., Jones, M. W., Andrew, R. M., Hauck, J., Olsen, A., ... Zaehle, S. (2020). Global Carbon Budget 2020. *Earth System Science Data*, *12*(4), 3269–3340. doi: 10.5194/essd-12-3269-2020

Gaubert, B., Stephens, B. B., Basu, S., Chevallier, F., Deng, F., Kort, E. A., ... Yin, Y. (2019). Global atmospheric CO2 inverse models converging on neutral tropical land exchange, but disagreeing on fossil fuel and atmospheric growth rate. *Biogeosciences*, *16*(1), 117–134. doi: 10.5194/bg-16-117-2019

GLOBALVIEW-CO2C13. (2009). *Cooperative Atmospheric Data Integration Project - d13C of Carbon Dioxide.* NOAA ESRL, Boulder, Colorado [Available on Internet via anonymous FTP to aftp.cmdl.noaa.gov, Path: products/globalview/co2c13].

Gonsamo, A., D'Odorico, P., Chen, J. M., Wu, C., & Buchmann, N. (2017). Changes in vegetation phenology are not reflected in atmospheric CO2 and 13C/12C seasonality. *Global Change Biology*, *23*(10), 4029–4044. doi: 10.1111/gcb.13646

Graven, H. D., Allison, C. E., Etheridge, D. M., Hammer, S., Keeling, R. F., Levin, I., ... White, J. W. (2017). Compiled records of carbon isotopes in atmospheric CO2 for historical simulations in CMIP6. *Geoscientific Model Development*, *10*(12), 4405–4417. doi: 10.5194/gmd-10-4405-2017

Graven, H. D., Keeling, R. F., Piper, S. C., Patra, P. K., Stephens, B. B., Wofsy, S. C., ... Bent, J. D. (2013, 9). Enhanced Seasonal Exchange of CO2 by Northern Ecosystems Since 1960. *Science*, *341*(6150), 1085–1089. doi: 10.1126/science.1239207

Harris, I., Osborn, T. J., Jones, P., & Lister, D. (2020). Version 4 of the CRU TS monthly high-resolution gridded multivariate climate dataset. *Scientific Data*, *7*(1), 1–18. doi: 10.1038/s41597-020-0453-3

Hauck, J., & Völker, C. (2015, 3). Rising atmospheric CO2 leads to large impact of biology on Southern Ocean CO2 uptake via changes of the Revelle factor. *Geophysical Research Letters*, *42*(5), 1459–1464. doi: 10.1002/2015GL063070

Heimann, M., Esser, G., Haxeltine, A., Kaduk, J., Kicklighter, D. W., Knorr, W., ... Würth, G. (1998). Evaluation of terrestrial carbon cycle models through simulations of the seasonal cycle of atmospheric CO2: First results of a model intercomparison study. *Global Biogeochemical Cycles*, *12*(1), 1–24. doi: 10.1029/97GB01936

Heimann, M., Keeling, C. D., & Tucker, C. J. (1989). A three dimensional model of atmospheric CO2 transport based on observed winds: 3. Seasonal cycle and

synoptic time scale variations. In *Aspects of climate variability in the pacific and the western americas* (pp. 277–303). American Geophysical Union (AGU). doi: 10.1029/GM055p0277

Heimann, M., & Körner, S. (2003). *The Global Atmospheric Tracer Model TM3* (Tech. Rep.). Max-Planck-Institut für Biogeochemie, Jena (Germany): Max-Planck-Institut für Biogeochemie.

Hurtt, G. C., Chini, L., Sahajpal, R., Frolking, S., Bodirsky, B. L., Calvin, K., ... Zhang, X. (2020). Harmonization of global land use change and management for the period 850-2100 (LUH2) for CMIP6. *Geoscientific Model Development*, *13*(11), 5425–5464. doi: 10.5194/gmd-13-5425-2020

Ito, A., Inatomi, M., Huntzinger, D. N., Schwalm, C., Michalak, A. M., Cook, R., ... Zhao, F. (2016, 12). Decadal trends in the seasonal-cycle amplitude of terrestrial CO2 exchange resulting from the ensemble of terrestrial biosphere models. *Tellus B: Chemical and Physical Meteorology*, *68*(1), 28968. doi: 10.3402/tellusb.v68.28968

Jeltsch-Thömmes, A., & Joos, F. (2020). Modeling the evolution of pulse-like perturbations in atmospheric carbon and carbon isotopes: The role of weathering-sedimentation imbalances. *Climate of the Past*, *16*(2), 423–451. doi: 10.5194/cp-16-423-2020

Joos, F., & Bruno, M. (1998, 6). Long-term variability of the terrestrial and oceanic carbon sinks and the budgets of the carbon isotopes 13 C and 14 C. *Global Biogeochemical Cycles*, *12*(2), 277–295. doi: 10.1029/98GB00746

Joos, F., Spahni, R., D. Stocker, B., Lienert, S., Müller, J., Fischer, H., ... Liu, Z. (2020). N2O changes from the Last Glacial Maximum to the preindustrial - Part 2: Terrestrial N2O emissions and carbon-nitrogen cycle interactions. *Biogeosciences*, *17*(13), 3511–3543. doi: 10.5194/bg-17-3511-2020

Jung, M., Schwalm, C., Migliavacca, M., Walther, S., Camps-Valls, G., Koirala, S., ... Reichstein, M. (2020). Scaling carbon fluxes from eddy covariance sites to globe: Synthesis and evaluation of the FLUXCOM approach. *Biogeosciences*, *17*(5), 1343–1365. doi: 10.5194/bg-17-1343-2020

Kalnay, E., Kanamitsu, M., Kistler, R., Collins, W., Deaven, D., Gandin, L., ... Joseph, D. (1996, 3). The NCEP/NCAR 40-Year Reanalysis Project. *Bulletin of the American Meteorological Society*, *77*(3), 437–471. doi:

10.1175/1520-0477(1996)077⟨0437:TNYRP⟩2.0.CO;2

Kaminski, T., Heimann, M., & Giering, R. (1998). A Global Scale Inversion of the Transport of CO2 Based on a Matrix Representation of an Atmospheric Transport Model Derived by Its Adjoint. In *Air pollution modeling and its application xii* (pp. 247–255). Boston, MA: Springer US. doi: 10.1007/978-1-4757-9128-0{_}26

Keeling, C. D. (1979, 1). The Suess effect: 13Carbon-14Carbon interrelations. *Environment International*, *2*(4-6), 229–300. doi: 10.1016/0160-4120(79)90005-9

Keeling, C. D., Chin, J. F. S., & Whorf, T. P. (1996, 7). Increased activity of northern vegetation inferred from atmospheric CO2 measurements. *Nature*, *382*(6587), 146–149. doi: 10.1038/382146a0

Keeling, C. D., Piper, S. C., Bacastow, R. B., Wahlen, M., Whorf, T. P., Heimann, M., & Meijer, H. A. (2001). Exchanges of atmospheric CO2 and 13CO2 with the terrestrial biosphere and oceans from 1978 to 2000. *I. Global aspects, SIO Reference Series, No. 01-06, Scripps Institution of Oceanography, San Diego*.

Keeling, C. D., Piper, S. C., Bacastow, R. B., Wahlen, M., Whorf, T. P., Heimann, M., & Meijer, H. A. (2005). Atmospheric CO2 and 13CO2 Exchange with the Terrestrial Biosphere and Oceans from 1978 to 2000: Observations and Carbon Cycle Implications. In I. T. Baldwin et al. (Eds.), *A history of atmospheric co2 and its effects on plants, animals, and ecosystems* (pp. 83–113). New York, NY: Springer New York. doi: 10.1007/0-387-27048-5{_}5

Keller, K. M., Lienert, S., Bozbiyik, A., Stocker, T. F., Churakova (Sidorova), O. V., Frank, D. C., ... Joos, F. (2017, 5). 20th century changes in carbon isotopes and water-use efficiency: tree-ring-based evaluation of the CLM4.5 and LPX-Bern models. *Biogeosciences*, *14*(10), 2641–2673. doi: 10.5194/bg-14-2641-2017

Kondo, M., Patra, P. K., Sitch, S., Friedlingstein, P., Poulter, B., Chevallier, F., ... Ziehn, T. (2020, 3). State of the science in reconciling top-down and bottom-up approaches for terrestrial CO2 budget. *Global Change Biology*, *26*(3), 1068–1084. doi: 10.1111/gcb.14917

Landschützer, P., Gruber, N., Bakker, D. C. E., & Schuster, U. (2014, 9). Recent variability of the global ocean carbon sink. *Global Biogeochemical Cycles*, *28*(9), 927–949. doi: 10.1002/2014GB004853

Landschützer, P., Gruber, N., Bakker, D. C. E., Stemmler, I., & Six, K. D. (2018, 2). Strengthening seasonal marine CO2 variations due to increasing atmospheric CO2. *Nature Climate Change*, *8*(2), 146–150. doi: 10.1038/s41558-017-0057-x

Lienert, S., & Joos, F. (2018, 5). A Bayesian ensemble data assimilation to constrain model parameters and land-use carbon emissions. *Biogeosciences*, *15*(9), 2909–2930. doi: 10.5194/bg-15-2909-2018

Lloyd, J., & Farquhar, G. (1994). C13 discrimination during CO2 assimilation by the terrestrial biosphere. *Oecologia*, *99*(3-4), 201–215. doi: 10.1007/BF00627732

Long, M. C., Stephens, B. B., McKain, K., Sweeney, C., Keeling, R. F., Kort, E. A., ... Wofsy, S. C. (2021, 12). Strong Southern Ocean carbon uptake evident in airborne observations. *Science*, *374*(6572), 1275–1280. doi: 10.1126/science.abi4355

Majkut, J. D., Carter, B. R., Frölicher, T. L., Dufour, C. O., Rodgers, K. B., & Sarmiento, J. L. (2014, 7). An observing system simulation for Southern Ocean carbon dioxide uptake. *Philosophical Transactions of the Royal Society A: Mathematical, Physical and Engineering Sciences*, *372*(2019), 20130046. doi: 10.1098/rsta.2013.0046

Masarie, K. A., Peters, W., Jacobson, A. R., & Tans, P. P. (2014, 12). ObsPack: a framework for the preparation, delivery, and attribution of atmospheric greenhouse gas measurements. *Earth System Science Data*, *6*(2), 375–384. doi: 10.5194/essd-6-375-2014

Menviel, L., & Joos, F. (2012, 3). Toward explaining the Holocene carbon dioxide and carbon isotope records: Results from transient ocean carbon cycle-climate simulations. *Paleoceanography*, *27*(1). doi: 10.1029/2011PA002224

Menviel, L., Joos, F., & Ritz, S. P. (2012). Simulating atmospheric CO2,13C and the marine carbon cycle during the Last Glacial-Interglacial cycle: Possible role for a deepening of the mean remineralization depth and an increase in the oceanic nutrient inventory. *Quaternary Science Reviews*, *56*, 46–68. doi: 10.1016/j.quascirev.2012.09.012

Menviel, L., Mouchet, A., Meissner, K. J., Joos, F., & England, M. H. (2015, 11). Impact of oceanic circulation changes on atmospheric δ13CO2. *Global Biogeo-*

chemical Cycles, *29*(11), 1944–1961. doi: 10.1002/2015GB005207

Mook, W. (1986, 8). 13C in atmospheric CO2. *Netherlands Journal of Sea Research*, *20*(2-3), 211–223. doi: 10.1016/0077-7579(86)90043-8

Müller, J., & Joos, F. (2020). Global peatland area and carbon dynamics from the Last Glacial Maximum to the present – A process-based model investigation. *Biogeosciences*, *17*(21), 5285–5308. doi: 10.5194/bg-17-5285-2020

Müller, J., & Joos, F. (2021). Committed and projected future changes in global peatlands-continued transient model simulations since the Last Glacial Maximum. *Biogeosciences*, *18*(12), 3657–3687. doi: 10.5194/bg-18-3657-2021

Peng, S., Ciais, P., Chevallier, F., Peylin, P., Cadule, P., Sitch, S., ... Zhao, H. (2015, 1). Benchmarking the seasonal cycle of CO2 fluxes simulated by terrestrial ecosystem models. *Global Biogeochemical Cycles*, *29*(1), 46–64. doi: 10.1002/2014GB004931

Peylin, P., Law, R. M., Gurney, K. R., Chevallier, F., Jacobson, A. R., Maki, T., ... Zhang, X. (2013). Global atmospheric carbon budget: Results from an ensemble of atmospheric CO2 inversions. *Biogeosciences*, *10*(10), 6699–6720. doi: 10.5194/bg-10-6699-2013

Piao, S., Liu, Z., Wang, Y., Ciais, P., Yao, Y., Peng, S., ... Wang, T. (2018). On the causes of trends in the seasonal amplitude of atmospheric CO2. *Global Change Biology*, *24*(2), 608–616. doi: 10.1111/gcb.13909

Quay, P. D., Sonnerup, R., Munro, D. R., & Sweeney, C. (2017, 1). Anthropogenic CO2 accumulation and uptake rates in the Pacific Ocean based on changes in the 13 C/ 12 C of dissolved inorganic carbon. *Global Biogeochemical Cycles*, *31*(1), 59–80. doi: 10.1002/2016GB005460

Ritz, S. P., Stocker, T. F., Joos, F., Ritz, S. P., Stocker, T. F., & Joos, F. (2011, 1). A Coupled Dynamical Ocean–Energy Balance Atmosphere Model for Paleoclimate Studies. *Journal of Climate*, *24*(2), 349–375. doi: 10.1175/2010JCLI3351.1

Saurer, M., Spahni, R., Frank, D. C., Joos, F., Leuenberger, M., Loader, N. J., ... Young, G. H. (2014, 12). Spatial variability and temporal trends in water-use efficiency of European forests. *Global Change Biology*, *20*(12), 3700–3712. doi: 10.1111/gcb.12717

Scholze, M., Ciais, P., & Heimann, M. (2008). Modeling terrestrial13C cycling: Cli-

mate, land use and fire. *Global Biogeochemical Cycles*, *22*(1), 1–13. doi: 10.1029/2006GB002899

Scholze, M., Kaplan, J. O., Knorr, W., & Heimann, M. (2003). Climate and interannual variability of the atmosphere-biosphere 13CO2 flux. *Geophysical Research Letters*, *30*(2), 1–4. doi: 10.1029/2002GL015631

Schürmann, G. J., Kaminski, T., Köstler, C., Carvalhais, N., Voßbeck, M., Kattge, J., ... Zaehle, S. (2016, 9). Constraining a land-surface model with multiple observations by application of the MPI-Carbon Cycle Data Assimilation System V1.0. *Geoscientific Model Development*, *9*(9), 2999–3026. doi: 10.5194/gmd-9-2999-2016

Seiler, C., Melton, J. R., Arora, V. K., Sitch, S., Friedlingstein, P., Anthoni, P., ... Zaehle, S. (2022, 4). Are terrestrial biosphere models fit for simulating the global land carbon sink? *Journal of Advances in Modeling Earth Systems*. doi: 10.1029/2021MS002946

Suess, H. E. (1955). Radiocarbon Concentration in Modern Wood. *Science*, *122*(3166), 415–417. doi: 10.1126/science.122.3166.415.b

Takahashi, T., Sutherland, S. C., Wanninkhof, R., Sweeney, C., Feely, R. A., Chipman, D. W., ... de Baar, H. J. (2009, 4). Climatological mean and decadal change in surface ocean pCO2, and net sea–air CO2 flux over the global oceans. *Deep Sea Research Part II: Topical Studies in Oceanography*, *56*(8-10), 554–577. doi: 10.1016/j.dsr2.2008.12.009

Tian, H., Yang, J., Lu, C., Xu, R., Canadell, J. G., Jackson, R. B., ... Zhu, Q. (2018, 6). The Global N2O Model Intercomparison Project. *Bulletin of the American Meteorological Society*, *99*(6), 1231–1251. doi: 10.1175/BAMS-D-17-0212.1

Tschumi, E., Lienert, S., Wiel, K. V. D., Joos, F., & Zscheischler, J. (2021). The effects of varying drought-heat signatures on terrestrial carbon dynamics and vegetation composition. *Biogeosciences Discussions*(July), 1–19.

Turnbull, J. C., Fletcher, S. E., Ansell, I., Brailsford, G. W., Moss, R. C., Norris, M. W., & Steinkamp, K. (2017). Sixty years of radiocarbon dioxide measurements at Wellington, New Zealand: 1954-2014. *Atmospheric Chemistry and Physics*, *17*(23), 14771–14784. doi: 10.5194/acp-17-14771-2017

Walker, A. P., De Kauwe, M. G., Bastos, A., Belmecheri, S., Georgiou, K., Keeling,

R. F., ... Zuidema, P. A. (2021). Integrating the evidence for a terrestrial carbon sink caused by increasing atmospheric CO2. *New Phytologist*, *229*(5), 2413–2445. doi: 10.1111/nph.16866

Wang, S., Zhang, Y., Ju, W., Chen, J. M., Ciais, P., Cescatti, A., ... Peñuelas, J. (2020, 12). Recent global decline of CO2 fertilization effects on vegetation photosynthesis. *Science*, *370*(6522), 1295–1300. doi: 10.1126/science.abb7772

Figure 1.

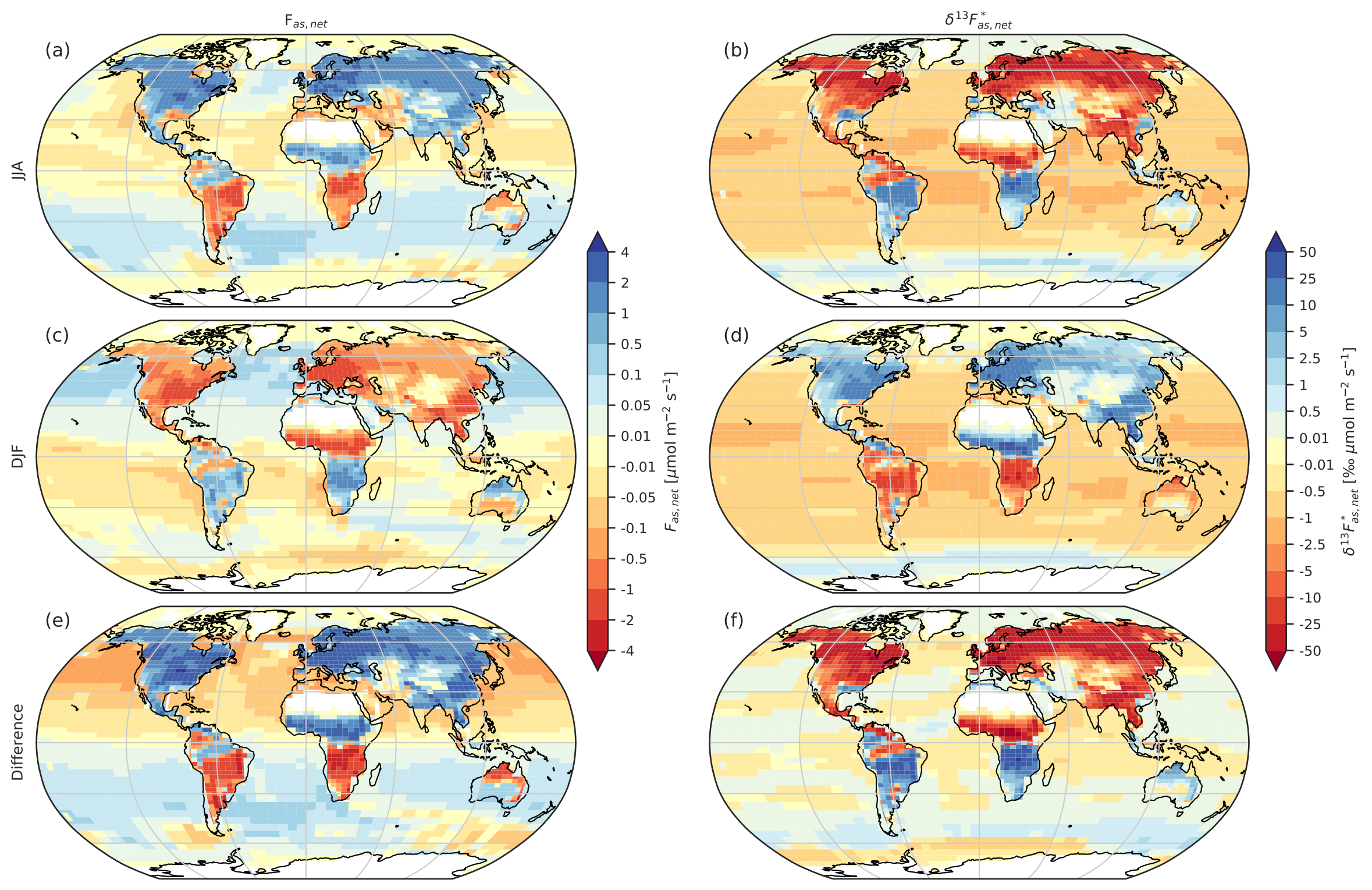
$F_{as,net}$
$\delta^{13}F^*_{as,net}$
(a)
(b)
(c)
(d)
(e)
(f)
JJA
DJF
Difference
4
2
1
0.5
0.1
0.05
0.01
-0.01
-0.05
-0.1
-0.5
-1
-2
-4
$F_{as,net}$ [μmol m^{-2} s^{-1}]
50
25
10
5
2.5
1
0.5
0.01
-0.01
-0.5
-1
-2.5
-5
-10
-25
-50
$\delta^{13}F^*_{as,net}$ [‰ μmol m^{-2} s^{-1}]

Figure 2.

Alert, Nunavut, Canada

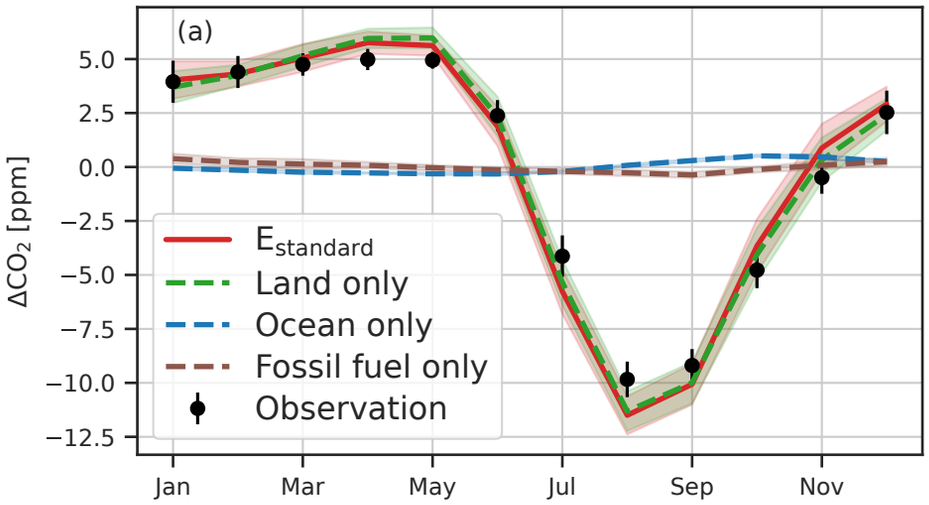

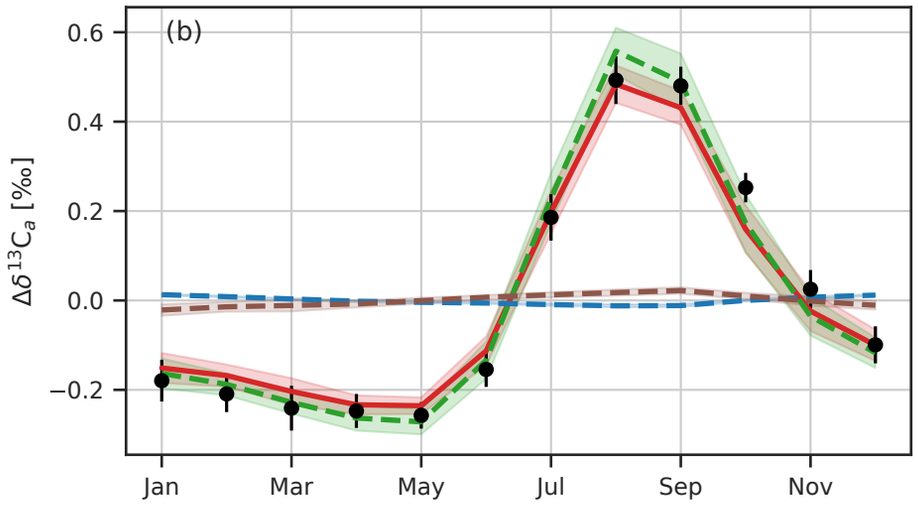

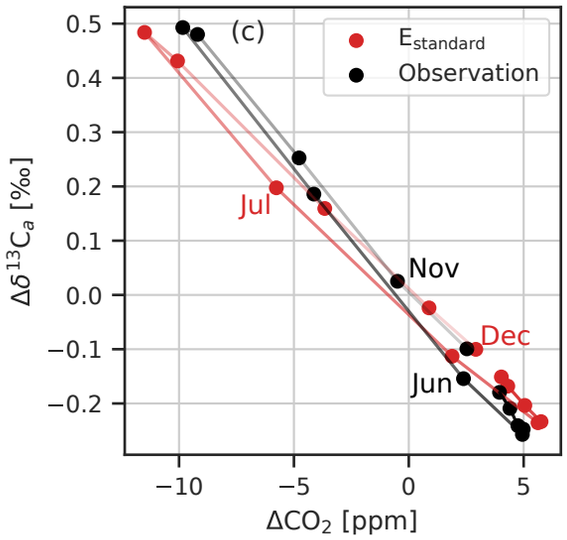

Mauna Loa, Hawaii, US

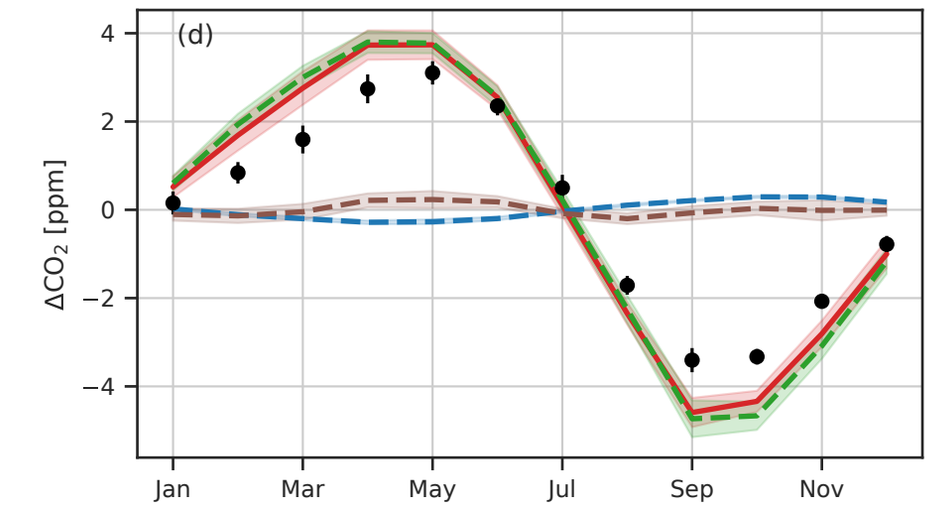

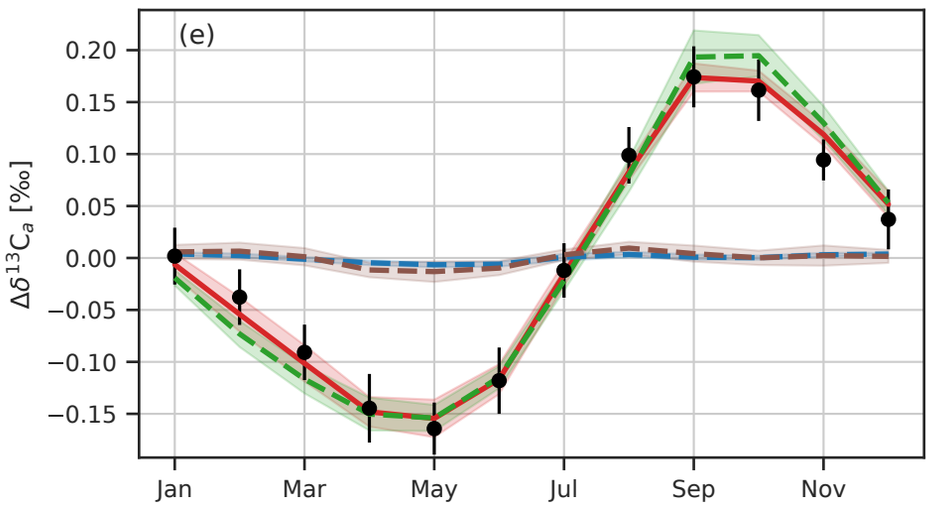

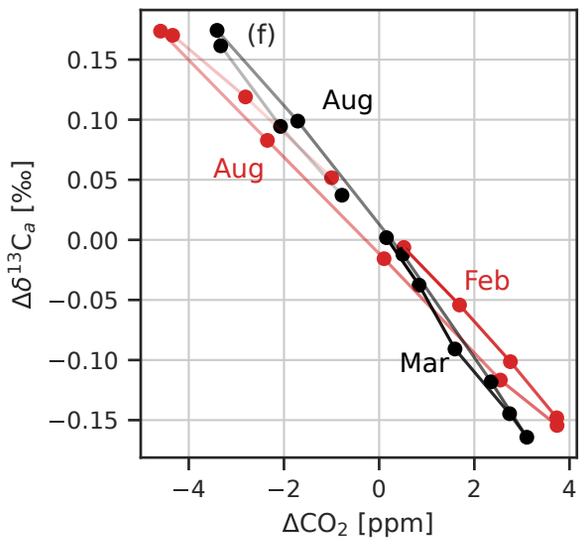

South Pole, Antarctica

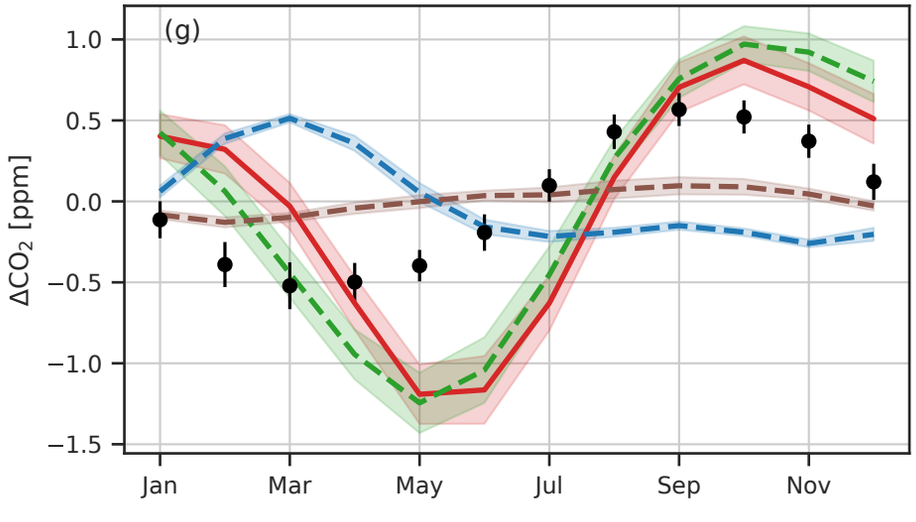

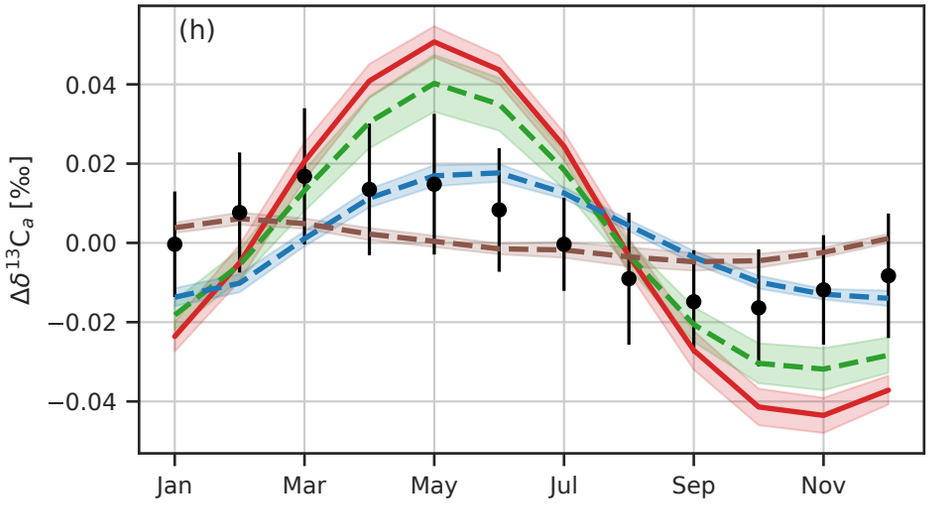

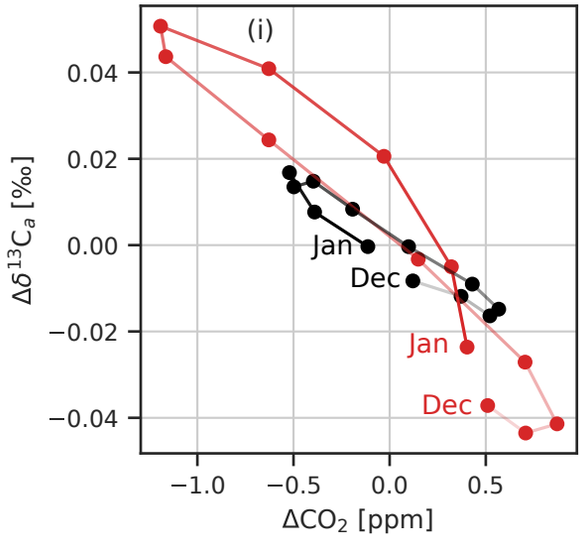

Figure 3.

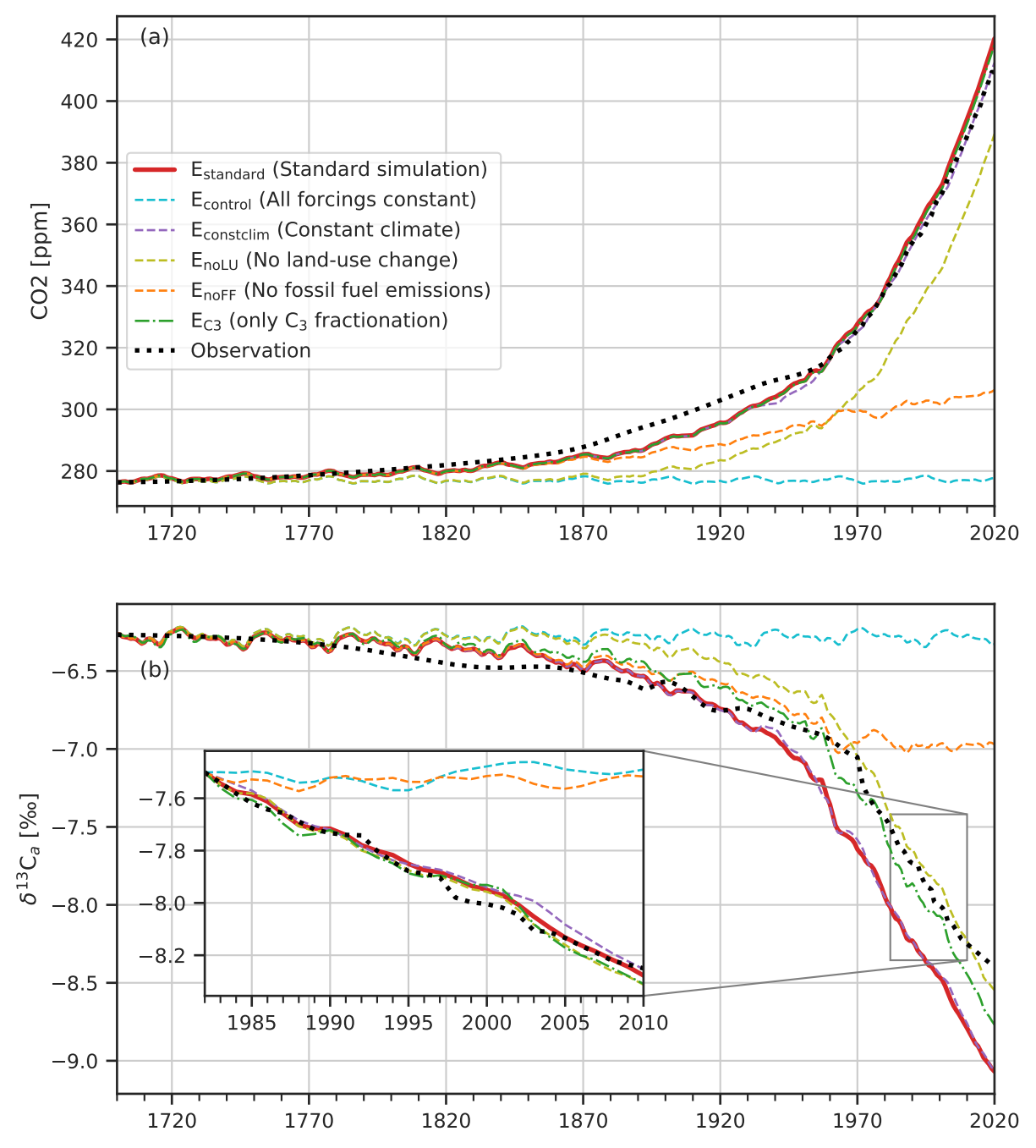
(a)
CO2 [ppm]
420
400
380
360
340
320
300
280
$E_{standard}$ (Standard simulation)
$E_{control}$ (All forcings constant)
$E_{constclim}$ (Constant climate)
E_{noLU} (No land-use change)
E_{noFF} (No fossil fuel emissions)
E_{C3} (only C_3 fractionation)
Observation
1720
1770
1820
1870
1920
1970
2020
(b)
$\delta^{13}C_a$ [‰]
−6.5
−7.0
−7.5
−8.0
−8.5
−9.0
−7.6
−7.8
−8.0
−8.2
1985
1990
1995
2000
2005
2010

Figure 4.

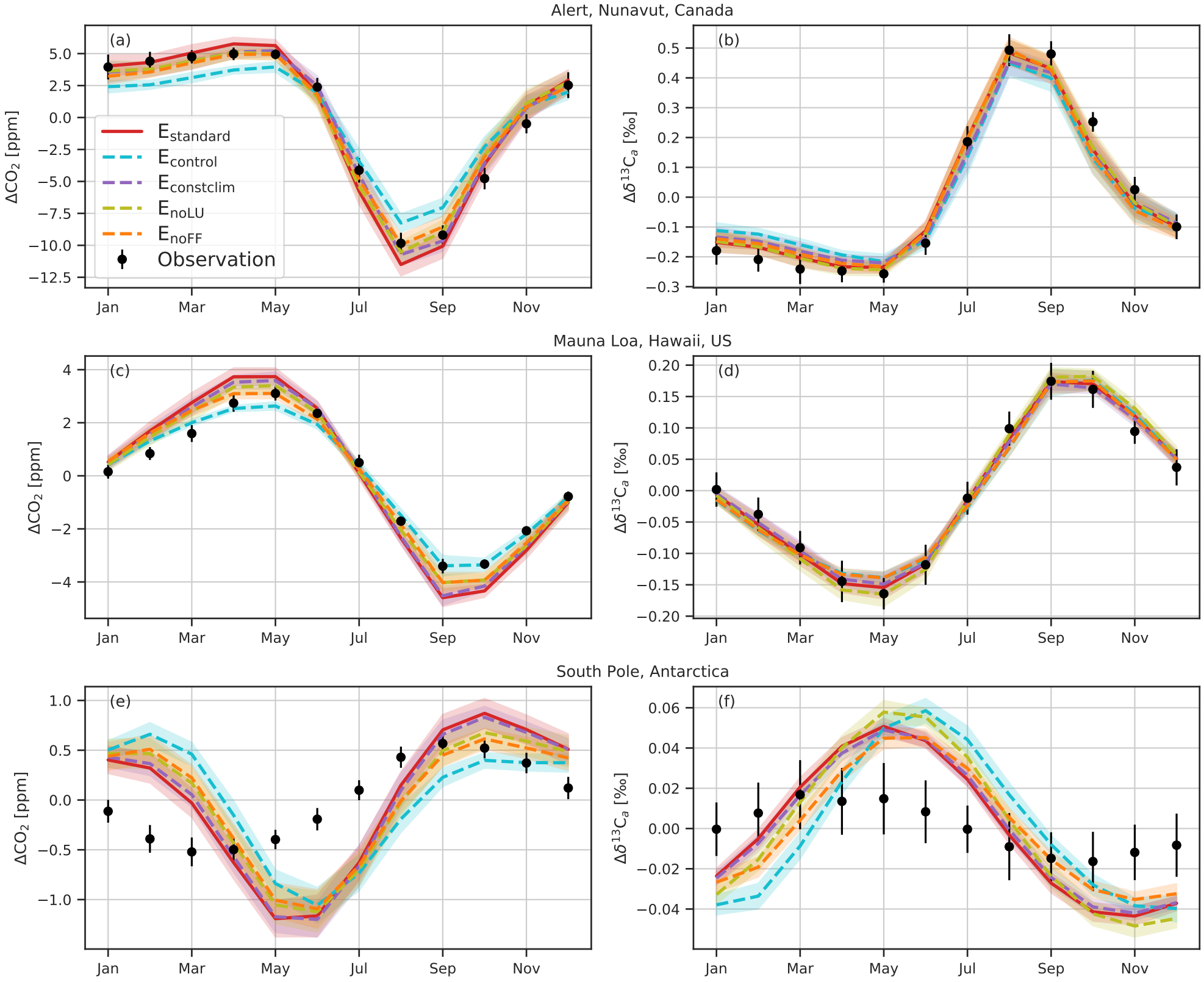
Alert, Nunavut, Canada
(a)
(b)
Mauna Loa, Hawaii, US
(c)
(d)
South Pole, Antarctica
(e)
(f)
ΔCO2 [ppm]
Δδ13Ca [‰]
E standard
E control
E constclim
E noLU
E noFF
Observation
Jan
Mar
May
Jul
Sep
Nov

Figure 5.

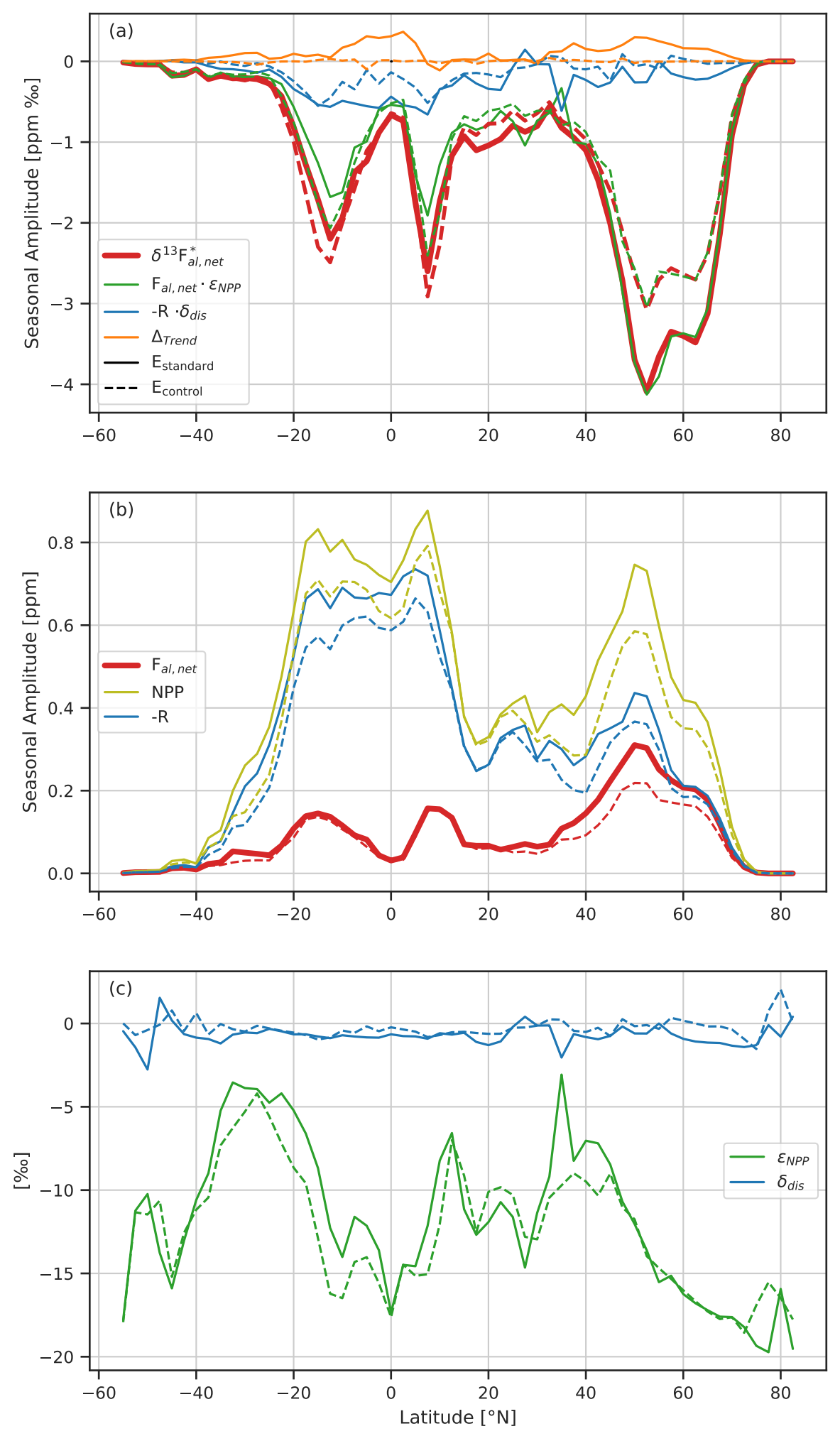
(a)
Seasonal Amplitude [ppm ‰]
$\delta^{13}F^{*}_{al,net}$
$F_{al,net} \cdot \varepsilon_{NPP}$
-R $\cdot\delta_{dis}$
Δ_{Trend}
$E_{standard}$
$E_{control}$
(b)
Seasonal Amplitude [ppm]
$F_{al,net}$
NPP
-R
(c)
[‰]
ε_{NPP}
δ_{dis}
Latitude [°N]

Supporting Information for "The seasonal cycle of δ^{13}C of atmospheric carbon dioxide: Influences of land and ocean carbon fluxes and drivers."

Sebastian Lienert[1,2], Sönke Zaehle[3], Fortunat Joos[1,2]

[1]Climate and Environmental Physics, University of Bern, Bern Switzerland

[2]Oeschger Centre for Climate Change Research, University of Bern, Bern, Switzerland

[3]Max Planck Institute for Biogeochemistry, P.O. Box 600164, Hans-Knöll-Str. 10, 07745 Jena, Germany

Contents of this file

August 19, 2022, 12:56pm

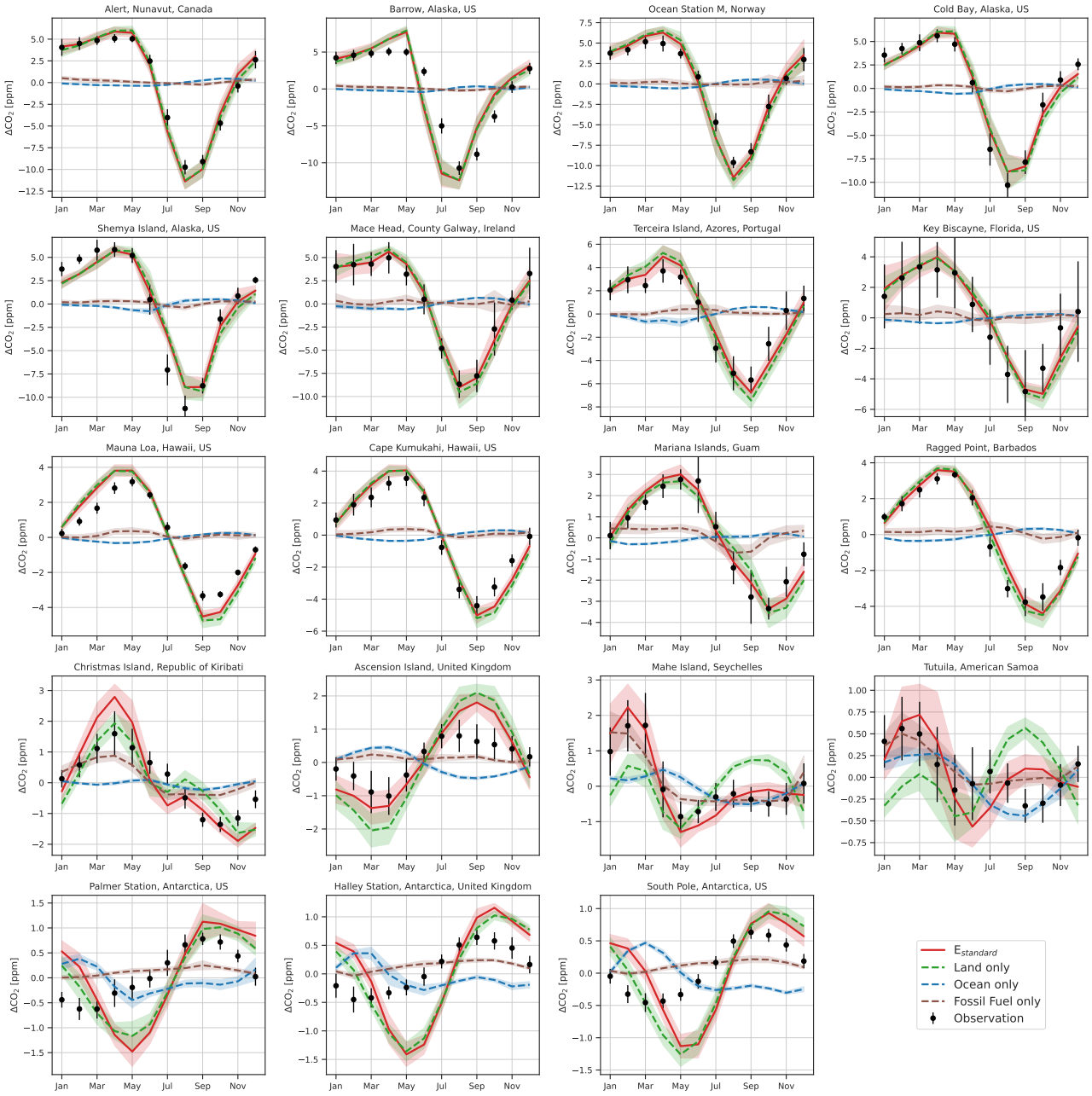

Figure S1. The seasonal cycle of CO_2 simulated by Bern3D-LPX and transported with TM3 (red), compared to observations (black dots). The calculation of the seasonal cycle only considers months between 1982 and 2012 where both the measurements and transport matrices are available. The location of the measurements is indicated in the title of the plot. The results of only transporting fluxes of terrestrial (green, dashed), oceanic (blue, dashed), and from fossil sources (brown, dashed) are shown with dashed lines. Error bars and shading correspond to the interannual standard deviation.

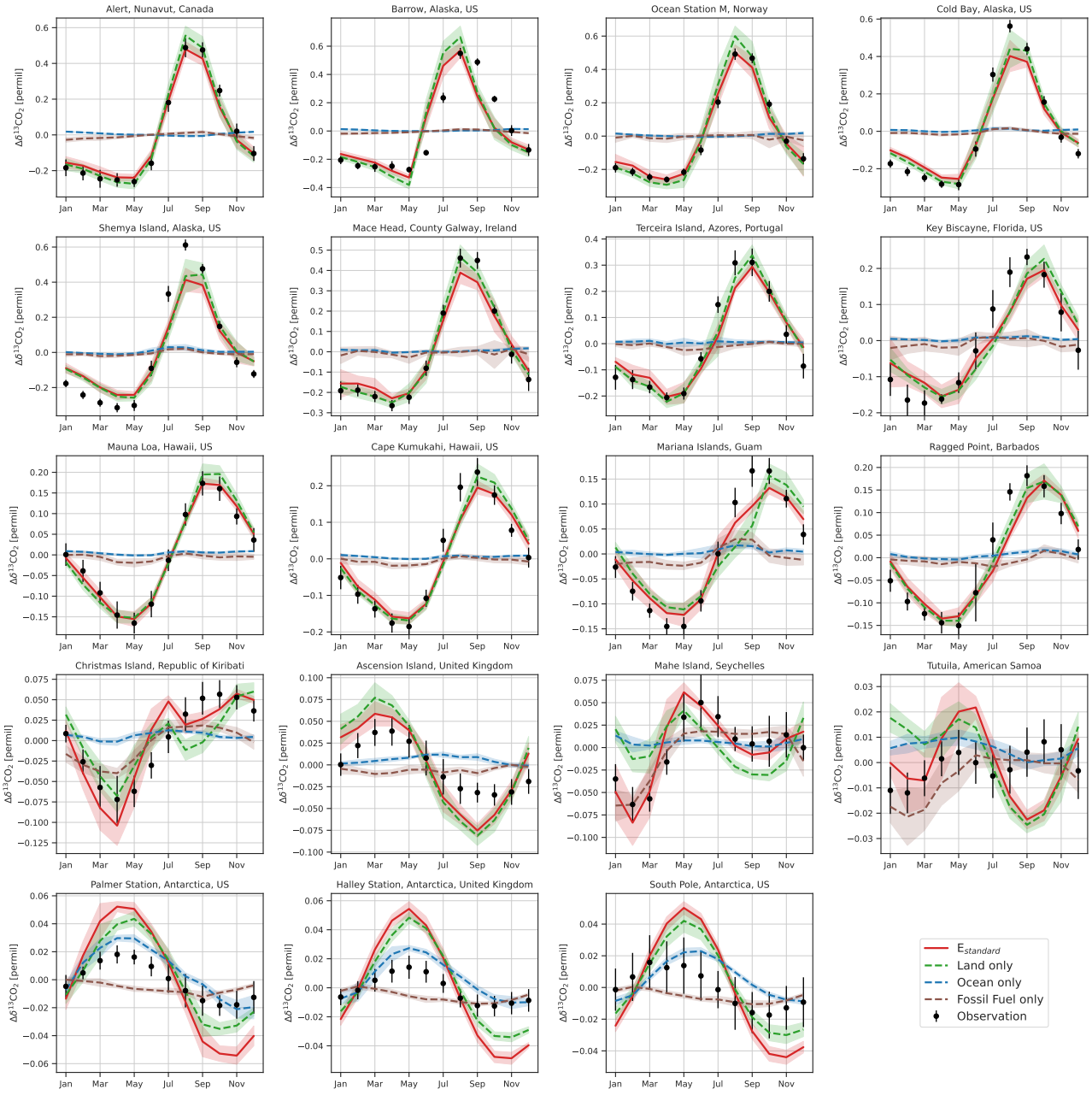

Figure S2. The seasonal cycle of $\delta^{13}C(CO_2)$ simulated by Bern3D-LPX and transported with TM3 (red), compared to observations (black dots). The calculation of the seasonal cycle only considers months between 1982 and 2012 where both the measurements and transport matrices are available. The location of the measurements is indicated in the title of the plot. The results of only transporting fluxes of terrestrial (green, dashed), oceanic (blue, dashed), and from fossil sources (brown, dashed) are shown with dashed lines. Error bars and shading correspond to the interannual standard deviation.

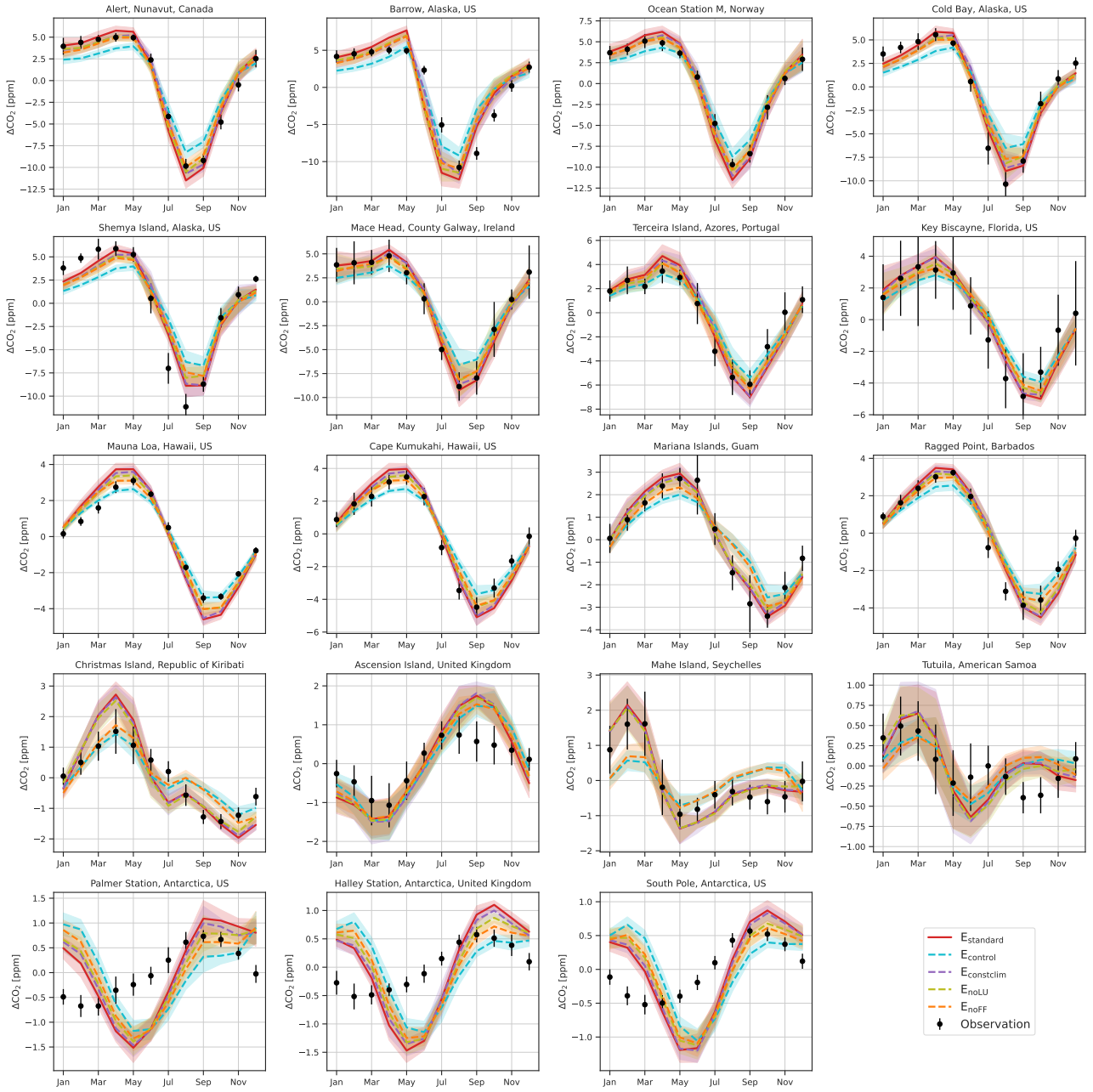

Figure S3. The seasonal cycle of CO_2 simulated by Bern3D-LPX and transported with TM3 (red), compared to observations (black dots). The calculation of the seasonal cycle only considers months between 1982 and 2012 where both the measurements and transport matrices are available. The results of sensitivity simulations are shown with dashed lines: $E_{control}$ (cyan,dashed), $E_{constclim}$ (purple, dashed), E_{noLU} (olive, dashed), and E_{noFF} (orange, dashed). Shading and error bars correspond to the interannual standard deviation.

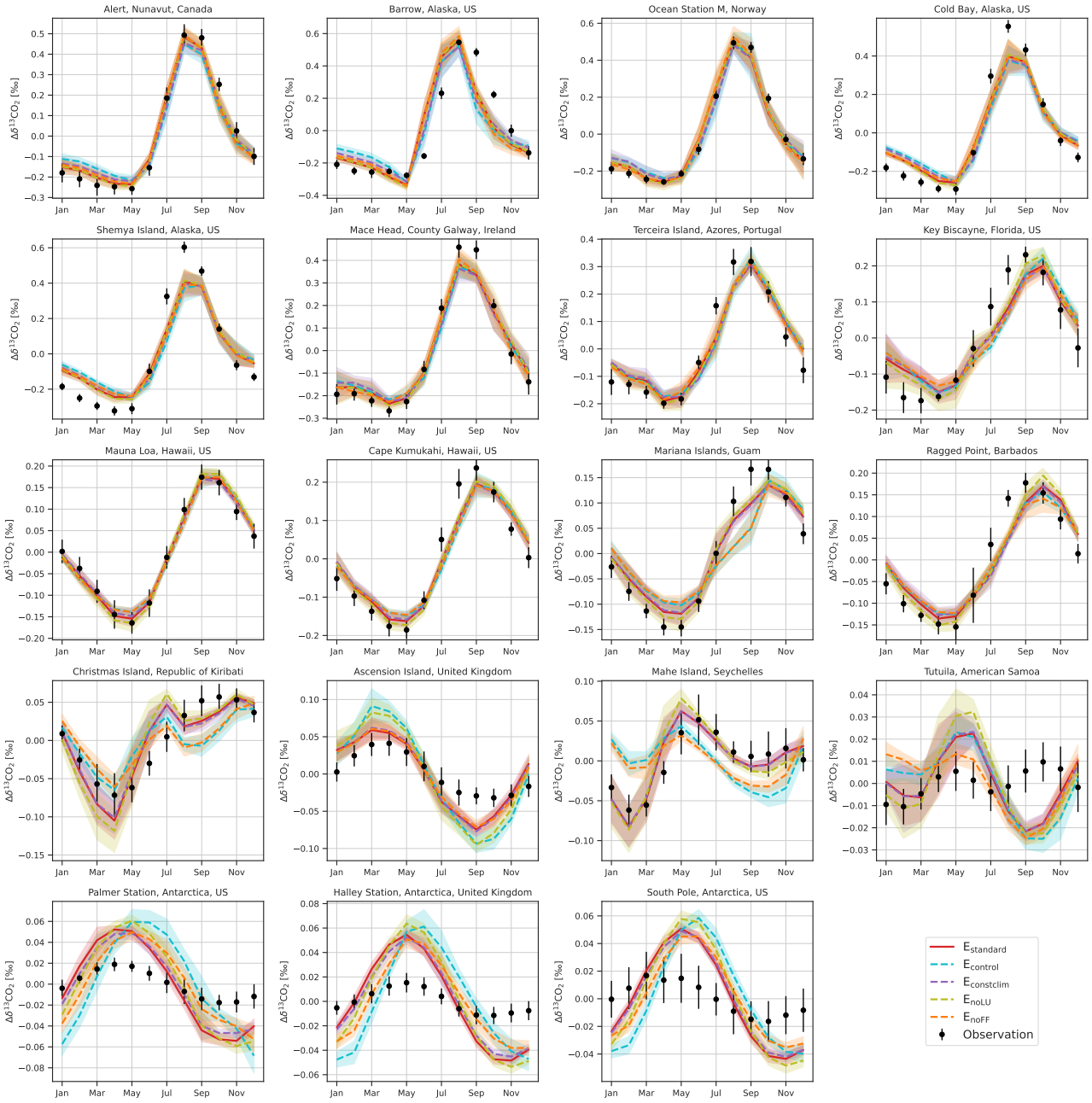

Figure S4. The seasonal cycle of $\delta^{13}C(CO_2)$ simulated by Bern3D-LPX and transported with TM3 (red), compared to observations (black dots). The calculation of the seasonal cycle only considers months between 1982 and 2012 where both the measurements and transport matrices are available. The results of sensitivity simulations are shown with dashed lines: $E_{control}$ (cyan,dashed), $E_{constclim}$ (purple, dashed), E_{noLU} (olive, dashed), and E_{noFF} (orange, dashed). Shading and error bars correspond to the interannual standard deviation.

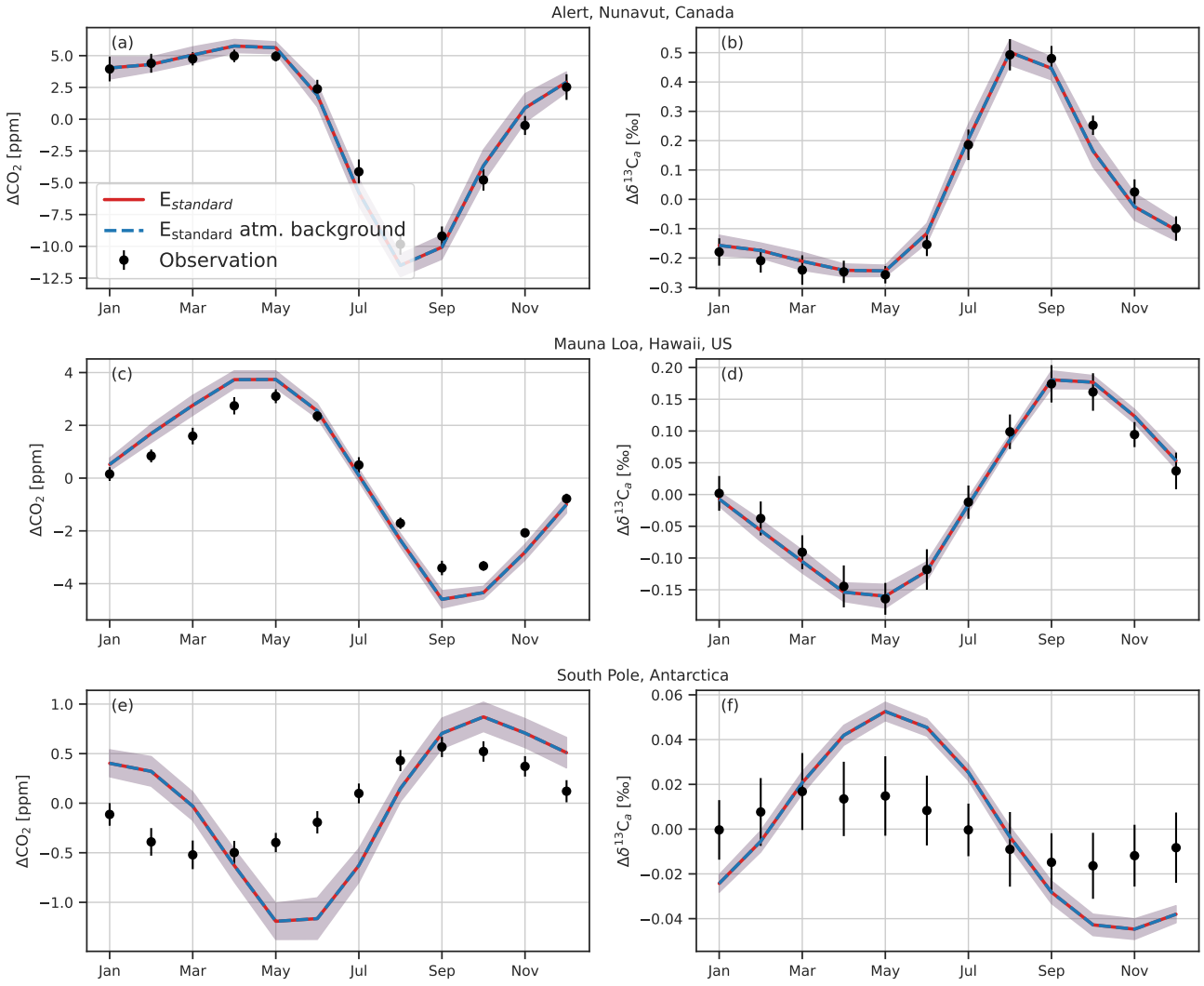

Figure S5. The seasonal cycle of CO_2 (left panels; (a,c,e)) and $\delta^{13}C_a$ (right panels; (b,d,f)) at Alert, northern Canada (a,b), Mauna Loa, Hawaii (c,d) and South Pole (e,f) as simulated by Bern3D-LPX and transported with TM3 (red), compared to observations (black dots). The calculation of the seasonal cycle only considers months between 1982 and 2012 where both the measurements and transport matrices are available. The result of running the transport model initialized with observed instead of simulated atmospheric concentration and signature is shown with dashed blue lines.

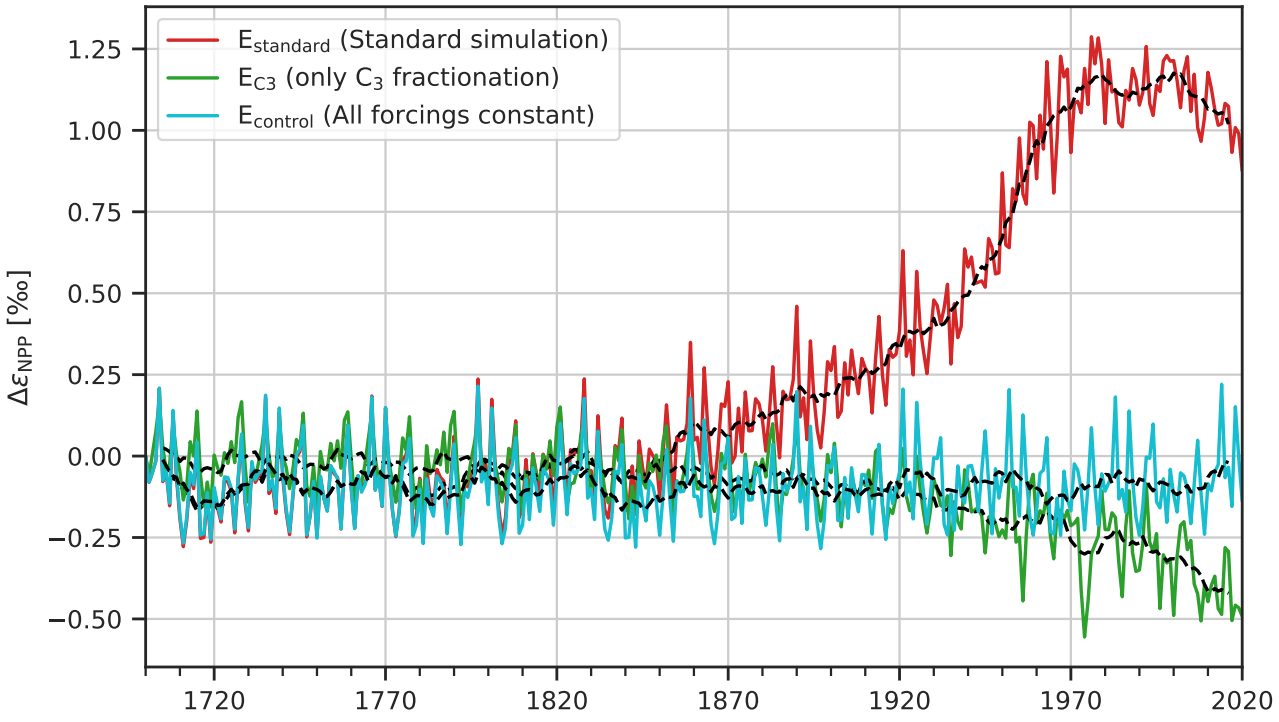

Figure S6. Simulated change in photosynthetic discrimination $\varepsilon_{\mathrm{NPP}}$ over the industrial period. The results of three simulations are shown: $\mathrm{E_{standard}}$ in red, $\mathrm{E_{C3}}$ and $\mathrm{E_{control}}$ in cyan. 10-year running means are indicated with black dashed lines.